Seismicity, fault architecture, and slip mode of the westernmost Gofar transform fault

Jianhua Gong[1] and Wenyuan Fan[2]

[1]Scripps Institution of Oceanography
[2]Scripps Institution of Oceanography, UCSD

November 21, 2022

Abstract

Oceanic transform faults accommodate plate motions through both seismic and aseismic slips. However, deformation partition and slip mode interaction at these faults remain elusive mainly limited by rare observations. We use one-year ocean bottom seismometer data collected in 2008 to detect and locate earthquakes at the westernmost Gofar transform fault. The ultra-fast slipping rate of Gofar results in ~30,000 earthquakes during the observational period, providing an excellent opportunity to investigate interrelations between the slip mode, seismicity, and fault architecture at an unprecedented resolution. Earthquake distribution indicates that the 100 km long Gofar transform fault is distinctly segmentated into five zones, including one zone contouring a M6 earthquake that was captured by the experiment. Further, a barrier zone east of the M6 earthquake hosted abundant foreshocks preceding the M6 event and halted its active seismicity afterwards. The barrier zone has two layers of earthquakes at depth, and they responded to the M6 earthquake differently. Additionally, a zone connecting to the East Pacific Rise had quasi-periodic earthquake swarms. The seismicity segmentation suggests that the Gofar fault has multiple slip modes occurring in adjacent fault patches. Spatiotemporal characteristics of the earthquakes suggest that complex fault architecture and fluid-rock interaction play primary roles in modulating the slip modes at Gofar, possibly involving multiple concurrent physical processes.

Seismicity, fault architecture, and slip mode of the westernmost Gofar transform fault

Jianhua Gong[1] **& Wenyuan Fan**[1]

[1]Scripps Institution of Oceanography, UC San Diego, La Jolla, California 92093, USA

Key Points:

- The westernmost Gofar transform fault is composed of distinct seismic and aseismic zones.
- These fault zones are controlled by different slip modes and they possibly interact with each other via multiple mechanisms.
- The slip mode variations may result from the complex fault architecture and fluid-rock interactions at multiple scales.

Corresponding author: Jianhua Gong, j4gong@ucsd.edu

Abstract

Oceanic transform faults accommodate plate motions through both seismic and aseismic slips. However, deformation partition and slip mode interaction at these faults remain elusive mainly limited by rare observations. We use one-year ocean bottom seismometer data collected in 2008 to detect and locate earthquakes at the westernmost Gofar transform fault. The ultra-fast slipping rate of Gofar results in ∼30,000 earthquakes during the observational period, providing an excellent opportunity to investigate interrelations between the slip mode, seismicity, and fault architecture at an unprecedented resolution. Earthquake distribution indicates that the ∼100 km long Gofar transform fault is distinctly segmentated into five zones, including one zone contouring a M6 earthquake that was captured by the experiment. Further, a barrier zone east of the M6 earthquake hosted abundant foreshocks preceding the M6 event and halted its active seismicity afterwards. The barrier zone has two layers of earthquakes at depth, and they responded to the M6 earthquake differently. Additionally, a zone connecting to the East Pacific Rise had quasi-periodic earthquake swarms. The seismicity segmentation suggests that the Gofar fault has multiple slip modes occurring in adjacent fault patches. Spatiotemporal characteristics of the earthquakes suggest that complex fault architecture and fluid-rock interaction play primary roles in modulating the slip modes at Gofar, possibly involving multiple concurrent physical processes.

Plain Language Summary

Oceanic transform faults are apparently simple tectonic plate boundaries. However, their structures are surprisingly complex as manifested through various seismic and aseismic slip modes. The deformation partition mechanism is not well understood due to a lack of near field observations. Here we use one-year long ocean bottom seismometer data to study earthquakes at the westernmost Gofar transform fault and use these earthquakes to infer the fault slip modes. Spatiotemporal evolution of the earthquakes suggests that the fault has five distinctive zones along strike, including one zone hosted a magnitude (M) 6 earthquake captured by the experiment. The remaining zones are dominated by either seismic or aseismic slip. Such distinct variations of slip mode along strike likely originate from the complex, heterogeneous fault structure and extensive fluid-rock interactions.

1 Introduction

Both seismic and aseismic slip can consume the total slip budget to accommodate plate motions (Avouac, 2015; Harris, 2017; Wolfson-Schwehr & Boettcher, 2019). The two slip modes dominate different fault patches and show variations along both the strike and dip directions (e.g, Scholz, 1998; Y. Liu & Rice, 2005; Han et al., 2017; Y. K. Liu et al., 2022). For example, earthquakes and slow earthquakes occur at subduction zone with different types of events dominating megathrust segments at varying depths (Lay et al., 2012; Obara & Kato, 2016; Wirth et al., 2022). Oceanic transform faults (OTFs) also slip in both modes with 15%–35% of the slip budget released through earthquakes and the rest as aseismic slips (Boettcher & Jordan, 2004; Y. Liu et al., 2012; Wolfson-Schwehr & Boettcher, 2019). The two slip modes at OTFs switch intermittently with variations predominately along the strike direction (McGuire et al., 2012; Shi et al., 2021). Moderate to large magnitude OTF earthquakes often repeatedly occur on isolate segments that are likely surrounded by creeping segments (e.g., Castellanos et al., 2020; Shi et al., 2021). For example, M6 earthquakes quasi-periodically rupturing the same fault patches has been observed at multiple OTF systems, including the Gofar transform fault system at the East Pacific Rise (McGuire, 2008; Braunmiller & Nábělek, 2008; Sykes & Ekström, 2012; Wolfson-Schwehr et al., 2014; Aderhold & Abercrombie, 2016). Such regular earthquake-cycle behaviors are rarely observed in other fault systems (Bakun et al., 2005). Further, these regular M6 earthquakes are frequently preceded with abundant foreshocks (McGuire et al., 2005, 2012; Aderhold & Abercrombie, 2016). These systematic patterns of OTF earthquakes suggest that their regulating physical processes are repeatable and the processes seem to be controlled by their slip modes and fault architecture. Therefore, understanding the slip modes as well as the fault architecture is critical in illuminating the underlining earthquake physics.

Fault architecture and slip mode partition are imprinted in microearthquakes (Vidale et al., 1994; Y. K. Liu et al., 2022). Particularly, interaction and triggering among different fault segments are often manifested as transient earthquake sequences lasting from seconds to years (Freed, 2005). For example, earthquakes can trigger afterslip to generate aftershocks (Hsu et al., 2006; Jiang et al., 2021), and accelerating aseismic slips are often accompanied by migrating earthquakes, which may eventually initiate large earthquakes (Shelly, 2009; Kato et al., 2012; McLaskey, 2019). Additionally, stress transfer and fluid migration can influence earthquakes at different fault segments over a large spatial footprint (e.g., Ross et al., 2020). Hence, investigating microearthquakes can help deciphering fault segmentation, slip partition, fault architecture, and mechanical controls of earthquake rupture dynamics (e.g., Hardebeck et al., 1998; Trugman et al., 2016; Y. K. Liu et al., 2022).

Despite OTFs exhibit some of the most predictable and systematic earthquake behaviors, details of their fault architecture and slip partition mechanisms are not well understood, mainly limited by rare near-field observations. However, remarkable details of the fault structures can be learned from microearthquakes when ocean bottom seismometer (OBS) data are available (McGuire et al., 2012; Wolfson-Schwehr et al., 2014; Kuna et al., 2019; Hicks et al., 2020; Yu et al., 2021; Gong et al., 2022). For example, barrier zones that separate repeated rupture patches are observed at Blanco and Gofar transform systems (McGuire et al., 2012; Kuna et al., 2019). Deep seismicity at 10–30 km are found from fast to slow slipping OTFs (Kuna et al., 2019; Yu et al., 2021; Gong et al., 2022), providing new insights into elastic failure conditions (Prigent et al., 2020; A. Kohli et al., 2021).

Previous studies usually report a few thousand earthquakes for an one-year OBS experiment (e.g., Kuna et al., 2019; Hicks et al., 2020). The catalog size may reflect challenges in picking emergent P waves and is also likely due to the coarse OBS array configurations (McGuire et al., 2012; Kuna et al., 2019; Hicks et al., 2020). Recent applications of machine-learning phase pickers to OBS data have produced multiple times more robust P and S phase picks than those from conventional approaches (Allen, 1978; Maeda, 1985; Saragiotis et al., 2002; Ruppert et al., 2021). For example, the advancement enables locating $\sim$24,000 earthquakes with a magnitude of completeness around 0.8 at the Quebrada transform fault system, revealing deep seismicity clouds that are likely controlled by aseismic slip and fluid circulation (e.g., Gong et al., 2022).

Here we investigate earthquakes at the westernmost segment of the Gofar transform system (G3) using one-year long OBS data collected in 2008 (McGuire et al., 2012). The deployment captured an anticipated M6 earthquake at G3 and recorded the end and early stages of an M6 earthquake seismic cycle. The experiment offers a unique opportunity to investigate the fault architecture, seismicity evolution, and their inter-relations in regulating earthquake rupture processes. Particularly, the active seismicity in the region provides a great opportunity to distinguish fault segmentation and the associated slip modes.

We apply a suite of techniques to detect, locate, and relocate earthquakes at G3 using the OBS data. Spatiotemporal evolution of the earthquakes suggests that the $\sim$100 km long Gofar fault has complex internal structures and is segmented into five zones with their seismicity dominantly but not exclusively influenced by one of the two slip modes. Further, deep seismicity is a common feature of the eastern G3 but absent at the western end, suggesting different temperatures and seismogenic depths along strike. Moreover, fault segments slipping aseismically have abundant microearthquakes. These segments are likely heavily damaged with heterogeneously distributed asperities, and their seismicity evolution implies intense fluid-rock interactions.

2 Gofar Transform Fault System

The Gofar transform fault system is located ∼4.4°S at the East Pacific Rise (EPR). It consists of three segments denoted as G1 to G3 from east to west that are connected by two short intra-transform spreading centers (ITSCs) (Pickle et al., 2009). Gofar transform fault system is at an ultra-fast spreading center that slips at a rate of ∼140 mm/yr (Wolfson-Schwehr & Boettcher, 2019). The Gofar faults have magnitude 5–6 earthquakes quasi-periodically at the same locations with a recurrence period of 5–6 years (McGuire, 2008; Wolfson-Schwehr et al., 2014).

The G3 fault branch shows clear along-strike variations in surface topography (Fig. 1). The western part of the fault connects to EPR, showing a "J"-shape structure with high elevation (Grevemeyer et al., 2021). Adjacent to the "J"-structure, there is a ∼10 km-long deep valley developed along the strike direction at ∼106°W with a maximum depth of ∼4100 m. The valley is bounded by high-elevation flanks on both the north and south sides of G3. The eastern topography of G3 is relatively simple with a linear shallow valley coinciding with the fault. The G3 fault connects a short ITSC at the east end, which has a lower elevation and a narrower width compared to EPR, indicating limited magma supply beneath the ITSC (Pickle et al., 2009).

Using the 2008 OBS data, McGuire et al. (2012) identified that G3 has fault patches with distinct seismicity characteristics. East of the M6 fault patch, there is a barrier zone that had intense seismicity from shallow to deep but halted the activity after the M6 mainshock. West of the M6 fault patch, a two-week long intense swarm occurred in December 2008 at a fault segment adjacent to EPR. The seismicity variation suggests the G3 fault patches slipping in different modes. Traveltime tomographic models show low Vp/Vs ratios in the barrier zone and high Vp/Vs ratios in the M6 rupture area, suggesting that the two patches have different fault zone materials (Guo et al., 2018; Froment et al., 2014). Long-term records reveal that M∼6 earthquakes rupture two sections of the G3 fault quasi-periodically (Shi et al., 2021). The western section is at the 2008 M6 earthquake zone and the other section is eastern of the barrier zone. The barrier zone is absent of M≥4 earthquakes, likely controlled by the aseismic slip mode (Wolfson-Schwehr et al., 2014; Shi et al., 2021).

3 Data and Methods

3.1 Data

The 2008 Quebrada-Discovery-Gofar marine seismic experiment deployed 30 broadband and 10 short-period three-component OBSs across the three fault systems with 16 broadband OBSs on the G3 segment, aiming to capture an anticipated M6 event (Fig. 1). Seven of the 16 OBS stations also had collocated strong motion sensors. The stations were situated in water depths ranging from 2960 m to 3930 m. The OBSs recorded waveform data at a sampling rate of either 50 Hz or 100 Hz (see Table S1 for details). Stations G01, G11, and G15 did not record useful data and we do not analyze their waveforms. During the experiment, an M6 event occurred on 18 September 2008 and triggered an M5 aftershock in the western section of the fault patch ∼20 min after the mainshock (Fig. 1). Another two M5 events occurred near the ridge-transform intersection in December as part of an energetic earthquake sequence.

3.2 Earthquake Detection, Location, and Magnitude Calculation

We follow Gong et al. (2022) to apply a four-step workflow to detect, associate, locate, and relocate earthquakes using open-source software (see Open Research). We first apply a machine-learning phase picker, EQTransformer, to detect P- and S-wave arrivals (Mousavi et al., 2020). EQTransformer is a deep-learning model that can simultaneously detect earthquakes and pick phase arrivals with uncertainty quantification. In our case, the waveforms of Gofar earthquakes have short S-P times than those used in the EQTransformer training dataset (Mousavi et al., 2019). Therefore, we upsample the data by a factor of 1 (no upsampling), 2 or 4 before applying EQTransformer (e.g., R. Wang et al., 2020; Gong et al., 2022). The upsampling factor is station-dependent and is determined through trial-and-error exercises by experimenting the factors on one-month long data at each station. The optimal upsampling factor is selected as the one yields most phase picks (see Table S1 for details). In total, we detect ∼515,000 P arrivals and ∼524,000 S arrivals.

The phase picks are then associated using REAL (Zhang et al., 2019). REAL grid searches for a candidate location and time to associate the phase picks by counting the number of P and S picks and computing the traveltime residuals. We require a successful association to have at least 3 P picks and 1 S picks and a residual arrival time tolerance of 0.5 s. The association uses a one-dimensional (1D) P-wave velocity profile (Fig. S1) extracted from a two-dimensional (2D) P-wave traveltime tomographic model of the Gofar system (Roland et al., 2012). A 1D S-wave velocity model is then converted from the 1D P-wave model by assuming a constant Vp/Vs ratio of 1.9 in the crust (above 6.85 km depth) and 1.8 in the mantle (below 6.85 km depth). Regions within 0.2° radius of the station that records the earliest phase arrival are searched with a depth extent up to 20 km. The searching regions are gridded at 0.01° horizontally and 0.5 km vertically. In total, we identify 47,220 candidate earthquakes from the association step.

We use COMPLOC to determine the earthquake absolute locations using the associated P- and S-wave arrival times (G. Lin & Shearer, 2006). The COMPLOC algorithm corrects a source-specific station term when solving for local earthquake locations, which can improve the location accuracy by empirically removing the systematic effects of three-dimensional velocity structures (Richards-Dinger & Shearer, 2000; G. Lin & Shearer, 2005). Additionally, we use ℓ_1 norm to evaluate the traveltime residuals which is insensitive to phase-pick outliers. Some earthquake locations cannot be resolved due to the station configuration, and they are erroneously placed at the seafloor (e.g., Gong et al., 2022). We have visually inspected waveforms of such earthquakes and conclude that these shallow earthquakes are likely mislocated. Therefore, we remove events within 1 km depth to the seafloor, apply the COMPLOC method to locate remaining events, and iterate this procedure 40 times till the final results are stable (Fig. S2). The procedure results 30,855 locatable events (Fig. 2).

The earthquake locations are further refined using waveform cross-correlation data. We apply the GrowClust relocation method to the differential times obtained from cross-correlating P and S waveforms of adjacent event pairs to achieve high-precision relative earthquake locations (Trugman & Shearer, 2017). We cross-correlate body waveforms of the closest 100 events with those of each earthquake to obtain the differential traveltimes. We successfully relocate 30,854 earthquakes in total (Fig. 2).

For the relocated earthquakes, local magnitudes (M_L) are calculated using three-component displacement waveforms. We first remove the instrument response and convolve the records with the Wood-Anderson instrument response. The waveforms are then filtered between 4–20 Hz and windowed from 1 s before to 5 s after the S arrivals. A peak amplitude (A) is calculated as the maximum root sum square of the windowed three-component displacements. We also measure the peak noise amplitude (A_N) using the same approach but apply to a window of 5 s to 2 s before the P arrivals. The local magnitude is computed as

$$M_L = \log_{10} A + 2.56 \log_{10} D - 1.67, \tag{1}$$

where D is the hypocenteral distance. We only keep a local magnitude estimate at a given station if the signal to noise ratio (A/A_N) is greater than 10. The final M_L of the earthquake is estimated as the median value of M_L computed for all the available stations, and we discard the magnitude estimate if less than 5 stations had qualified measurements. We eventually obtain M_L for 6,164 earthquakes. The magnitude-frequency distribution of these earthquakes is shown in Fig. S3a. The magnitudes are unusually small. It is likely that the coefficients in Eq. 1 are different for Gofar as they were derived for southern California. Therefore, we calibrate our local magnitude estimates by using the moment magnitudes derived from displacement spectrum (Moyer et al., 2018). We apply a constant shift of 0.65 to our local magnitude estimates (see Text S1). The final catalog has a magnitude completeness of 0.6 and a b-value of 0.75 obtained from the maximum curvature method and maximum likelihood method respectively (Fig. S3c; Aki, 1965; Wiemer & Wyss, 2000).

3.3 Earthquake Clustering

In addition to solving for relative locations, GrowClust applies a hierarchical clustering algorithm that clusters events based on waveform cross-correlation coefficients (Trugman & Shearer, 2017). The algorithm first defines a similarity coefficient that serves as a metric to measure waveform similarity between event pairs, and then forms earthquake clusters based on the similarity coefficients (Trugman & Shearer, 2017). A cluster represents a set of events that are spatially close and have similar waveforms, which indicate that they might come from the same fault patch and share similar focal mechanisms. The number of clusters for a given catalog is influenced by the GrowClust parameters. We have experimented with seven sets of input parameters, and the results of each set are described in Text S2. We opt to a set of parameters that generates few off-fault clusters and are free from unrealistic gaps between seismicity strands (Fig. S4 and S5). The set of parameters leads to 34 clusters, and each cluster has more than 100 events (Fig. S6). These clusters include 84% of the total seismicity (Table S2). We focus on these 34 clusters in the following analysis. We further inspect the temporal behaviors of the clusters that are adjacent to each other and merge clusters if they show similar evolution in seismicity rate (Fig. S7).

3.4 Locating Missing Earthquakes

Visual inspection of daily waveforms suggests that there are missing events in the automated earthquake catalog, which have clear, large amplitudes. For example, the M6 mainshock and the M5 aftershock are missing from the catalog (Fig. S8). We speculate that the these events are missed because the training datasets of EQTransformer have limited near-field waveforms of $M \geq 5$ events (Mousavi et al., 2019). Further, Gofar earthquakes tend to generate emergent arrivals on OBS, posing challenges in detecting body waves using such phase pickers. Finally, the iterative location procedure also removes 35% events in the COMPLOC location step (Fig. S2).

In recognizing these challenges, we examine continuous waveforms to search for missing events whose amplitudes exceed a threshold of $\sim 1.2\times10^{-4}$ m/s (74,866 unit count) at more than one stations (see Text S1 for details). Specifically, 397 events are manually identified through this approach including the M6 mainshock, its largest aftershock, and two M5 events during the December swarm (Fig. S8). We hand pick their P and S arrivals and then locate these events using a grid-search procedure. We search a region from -4.75° to -4.4° in latitude and from -106.4° to -105.5° in longitude, with a grid spacing of 0.01° in both horizontal directions, respectively. The event depth is searched from 0 to 15 km, with an inter-grid spacing of 0.5 km. The misfit ($E(i)$) at the ith searching grid is defined as

$$E(i) = \sum_j \left| \overline{T}_X^{pre}(i,j) - \overline{T}_X(j) \right| \tag{2}$$

where $\overline{T}_X^{pre}(i,j)$ is the demeaned predicted P- or S-wave travel time from grid-i to station-j, and $\overline{T}_X(j)$ is the demeaned observed P- or S-wave arrival time at station-j. The demeaned travel times are defined as

$$\overline{T}_X^{pre}(i,j) = T_X^{pre}(i,j) - \frac{1}{N}\sum_k T_X^{pre}(i,k) \tag{3}$$

and

$$\overline{T}_X(j) = t_X(j) - \frac{1}{N}\sum_k t_X(k) \tag{4}$$

where $T_X^{pre}(i,j)$ and $t_X(j)$ are the predicted and observed P- or S-wave travel times from grid-i to station-j, respectively, and N is the number of available stations. The predicted P- or S-wave travel time is calculated using the same velocity model as being used for COMPLOC locations. The best location estimate yields the minimum misfit. We consider the event depth cannot be constrained when the depth is placed shallower than 1 km or deeper than 12 km. In such cases, the event depth is assigned as 5 km. The final locations of these events are shown in Fig. S9. We do not relocate these events because their waveforms are dissimilar to those of nearby small magnitude earthquakes. Earthquake magnitudes of these earthquakes are calculated in the same way as for earthquakes in the automated catalog.

3.5 Coulomb stress change

To understand inter-relations of the earthquake sequences, we compute Coulomb stress changes due to the M6 mainshock imposed on other G3 fault patches (King et al., 1994; Stein et al., 1997; J. Lin & Stein, 2004; J. Wang et al., 2021). No finite-fault model is available for this earthquake. Therefore, we assume a uniform slip model rupturing a rectangular fault patch with a length of 14.8 km and a width of 3.6 km in the mainshock zone (see Section 4). The rupture area is estimated using its aftershock distribution (Fig. 6). The fault geometry, including the strike, dip, and rake, of both the source fault and the receiver fault are 102°, 90°, and 0°. We also assume the earthquake with a moment magnitude of 6.0 and the fault with a shear modules of 40 GPa, which leads to an average slip of 0.6 m on the assumed slipping area. Result of Coulomb stress changes at various depths are shown in Fig. S10. The stresses are computed assuming a frictional coefficient of 0.4.

4 Results

Seismicity at G3 shows strong spatial and temporal variations in both the along-strike and along-dip (depth) directions. Based on these variations, we group the 34 clusters into five zones along strike. Clusters in the same zone have similar seismicity evolution (Table S3). The five zones are numbered 1 to 5 from east (ITSC) to west (EPR). In general, the seismicity trends agree well with the surface fault traces (Fig. 2). Majority of earthquakes (60%) are located in between 4 to 7 km in depth (Fig. 2). We consider earthquakes shallower than 7 km are crustal events and the deeper ones are upper-mantle earthquakes, following the 1D velocity model used for earthquake locations. Two prominent seismicity sequences occurred during the deployment, namely, the September M6 foreshock-mainshock-aftershock sequence in Zone 2 and 3 and the December swarm sequence in Zone 5 (Fig. 3). The characteristics of the five zones are detailed below.

4.1 Zone 1: Eastern Locked Zone

The easternmost G3 segment (Zone 1) connects to an ITSC, and Zone 1 spans about 30 km along strike (Fig. 4). For the past two decades, there were 11 M5–6 earthquakes occurring every 5–6 years in Zone 1 (Wolfson-Schwehr & Boettcher, 2019; Shi et al., 2021). Most of the microearthquakes in the region have local magnitudes less than 3. These events are located deeper than 4 km, roughly forming two separate layers. Earthquakes in the shallow layer (4–7 km) organize into sporadic patches, while earthquakes in the deep layer (7–10 km) concentrate at a $\sim$9 km depth forming a continuous linear streak along strike (Fig. 4). In combination with the spatial pattern, the temporal characteristics of earthquakes in Zone 1 suggest that they can be divided into two groups. The first group includes the shallow layer of seismicity and the easternmost patch of earthquakes (including events deeper than 7 km), which has a near-constant seismicity rate (Group 1, Fig. 4c). The second group contains most of the deep layer earthquakes, and they occur as intermittent bursts during the OBS deployment period (Group 2, Fig. 4d), with each burst lasting for about $\sim$2 days.

4.2 Zone 2: Barrier Zone

Adjacent to Zone 1, Zone 2 extends 10 km westward to the M6 rupture zone (Fig. 5). Zone 2 was denoted as the barrier zone in McGuire et al. (2012) as this fault segment may have involved in both nucleating and terminating the 2008 M6 Gofar earthquake (McGuire et al., 2012). The fault segment experienced abundant foreshocks before the M6 mainshock and a sudden shutdown of seismicity after the M6 mainshock. Earthquakes in Zone 2 are fragmented into two layers along dip (depth). From seafloor morphological features, these two layers may represent two fault branches. The shallow-layer earthquakes are located in between 2 and 6 km. Seismicity in the shallow layer was energetic prior to the M6 mainshock but absent after the mainshock. There was also a 7-day foreshock sequence in the shallow layer, including three M$\sim$4 foreshocks (Fig. S8). These shallow-layer earthquakes are termed as Group 1 events of Zone 2. The deep layer earthquakes are located in between 7 and 8 km and these events can be further divided into two groups (Group 2 and 3, Fig. 5). Group 2 is adjacent to the mainshock zone and its seismicity shows a similar temporal evolution as of Group 1. In contrast, intermittent earthquake bursts occurred in Group 3 before the M6 mainshock and continued after the mainshock, distinguishing itself from the other two groups in Zone 2.

4.3 Zone 3: 2008 M6 Mainshock Zone

The 2008 M6 Gofar earthquake occurred in Zone 3, west of Zone 2. This segment of the Gofar fault is also termed as the mainshock zone in McGuire et al. (2012). Zone 3 extends about 15 km along strike. The M6 mainshock initiated at the western edge of Zone 3 with its epicenter located at 106.1°W/4.54°S at a depth of 6 km. Majority of the earthquakes (80%) in Zone 3 occurred in between 4 and 7 km in depth, forming Group 1 of Zone 3. Group 1 contains most of the aftershocks, which seismicity rate follows a typical Omori-decay pattern (Fig. 6c). In conjunction with the M6 epicenter, the spatial footprint of the aftershocks indicates that the M6 mainshock ruptured eastward with an area of $\sim$60 km^2, a $\sim$15 km length along strike and a $\sim$4 km width along dip. This leads to a stress drop estimate of about 4 MPa for the M6 earthquake, assuming a rectangular rupture model. Earthquakes below 7 km form another two groups of Zone 3, including an eastern streak (Group 2) and a western deep pocket of seismicity (Group 3). Group 2 comprises both short episodes of foreshocks and aftershocks of the mainshock (Fig. 6d). Microearthquakes in Group 3 suggest a westward dipping structure between 6–8 km, occurring as intermittent bursts (Fig. 6e).

4.4 Zone 4: Transition Zone

Zone 4 extends ∼12 km west of Zone 3. During the 2008 experiment, the largest aftershock (a M5 event) is located at the western end of Zone 4 (Fig. 7). Earthquakes in Zone 4 occurred continuously during the experiment and their activity strongly correlates with both the M6 mainshock in Zone 3 and the December swarm sequence in Zone 5 (Fig. 7). Seismicity is distributed in between 4 and 7 km depth without deep earthquakes, forming multiple streaks. Given the seafloor morphological features, seismicity similarity coefficients, and earthquake spatiotemporal patterns, events in Zone 4 are further divided into three groups (Fig. 7). These three groups likely originate from three fault strands that are connected by two stepovers, matching seafloor topographic trends (Fig. 7a). The active seismicity in Zone 4 lasted for about at least three months after the mainshock. The influences of the M6 mainshock from the east and the December swarm sequence from the west correlate with their distances to the three groups (Fig. 7c–e).

4.5 Zone 5: Swarm Zone

The westernmost segment of G3 (Zone 5) connects the transform fault to EPR. There was a surge of earthquakes from December 6th to 20th in 2008 which is termed as the December swarm in McGuire et al. (2012). All earthquakes in Zone 5 are shallower than 7 km and are distributed in between 2 and 6 km in depth. These earthquakes can be divided into two groups based on their temporal behaviors (Fig. 8). Group 1 includes quasi-periodic swarms occurring every 24.4 days throughout the year. The periodicity of these swarms seems to be perturbed by the M6 mainshock in September (Fig. 8c). Group 2 is a spatially compact cluster located at ∼5 km depth extending ∼2 km in radius (Fig. 8d). Few earthquakes occurred in Group 2 prior to the December swarm, indicating a casual relation between the Group 2 earthquakes and the December swarm.

5 Discussion

5.1 Seismicity, Fault Architecture, and Slip Mode

The westernmost branch of the Gofar transform fault system (G3) is segmented into five distinct zones, and their seismicity characteristics indicate that different zones might operate under different stress states and/or have different geometric, material, and mechanical properties. We infer that fault slip modes of G3 switch between seismic and aseismic along strike and each fault segment is primarily controlled by one of the two slip modes. Further, along-dip segmentation and deep seismicity seem to be common features of the eastern part of G3, Zone 1, 2, and 3, although their controlling physical mechanisms likely differ from zone to zone.

5.1.1 Sporadic Locked Fault Patches

Characteristic M6 earthquakes have repeatedly ruptured Zone 1 and 3 for the past few decades with the 2008 M6 Gofar earthquake rupturing Zone 3 (McGuire et al., 2012; Shi et al., 2021). Microearthquakes are absent in the shallow portions (≤4 km) of these two zones with most of the seismicity located between 4–7 km in depth (Fig. 4 and 6). Seismicity delineates linear features that agree well with the surface fault traces, suggesting relatively simple fault-zone structures along strike. Therefore, plate motion is likely accommodated by seismic slip as the primary means at these two zones. The crustal portions of the fault patches are locked during the interseismic period with few microearthquakes, which down-dip edges are contoured by microseismicity in the lower-crust (4–7 km). Such seismicity distributions are similar to some locked continental faults that aftershocks primarily surround the mainshock rupture areas (Chan & Stein, 2009; Brocher et al., 2015).

There are three apparent fault branches in Zone 4 with an average fault length of ∼5 km and an average separation distance of ∼1 km (Fig. 7). Similar to Zone 1 and 3, there is a lack of seismicity in the shallow portion of the faults (≤4 km), and most microearthquakes likely occurred at the lower-crust depth (4–7 km). The largest aftershock of the 2008 mainshock, a M5 event, likely ruptured one of the three fault branches. The observations suggest that Zone 4 shares similarities with Zone 1 and 3 with plate motion primarily accommodated by seismic slips. However, its fault architecture has three sub-parallel strands and is more complex than those of Zone 1 and 3. The fault dimension likely controls the nominal magnitude of earthquakes in Zone 4 (Wolfson-Schwehr & Boettcher, 2019). Further, the geometric complexity of the three-fault network may have posed a western rupture boundary for M6 earthquakes in Zone 3, e.g., preventing the 2008 mainshock to propagate westward. However, the short stepovers are less than 5 km and they cannot stop an energetic rupture propagation (Barka & Kadinsky-Cade, 1988; Harris & Day, 1999; Wesnousky, 2008), which is in contrast to the current observations. Therefore, additional mechanical or material variations between Zone 3 and 4 might have contributed to prevent M6 earthquakes rupturing into Zone 4.

Earthquakes in Zone 4 are strongly influenced by both the M6 mainshock in Zone 3 and the December swarm in Zone 5. The microseismicity rate increased after the M6 mainshock and remained at a higher-than-background level for about three months. The December swarm caused another surge of seismicity in Zone 4, lasting till the end of the experiment. These earthquakes are likely triggered by the the mainshock and the December swarm. The lengthy duration (four months) indicates that non-linear triggering mechanisms might have controlled the triggered seismicity. For example, the M6 mainshock may have caused afterslip, viscoelastic relaxation, or poroelastic relaxation at the crust-mantle boundary, driving the triggered seismicity (Savage & Prescott, 1978; Marone et al., 1991; Segall & Lu, 2015). The December swarm might represent a transient aseismic slip event propagating from west to east, causing the surge of seismicity in Zone 4 (Fig. 9). Alternatively, fluid migration could have also caused the long-lasting triggered sequences (Ross et al., 2020; Ross & Cochran, 2021). In this case, the lower crust may have pervasive fluid pathways. The high sensitivity of Zone 4 to adjacent fault patches and its complex fault architecture suggest that Zone 4 might be a transition zone with a mélange locking structure in between predominantly seismic (Zone 3) and aseismic (Zone 5) fault segments.

5.1.2 Fault Damage Zone as A "Double Agent"

We record intense earthquake activity in Zone 2 starting from the beginning of the 2008 OBS deployment, which abruptly shut down after the M6 mainshock (Fig. 5). The mainshock was preceded by a foreshock sequence in the Zone 2 seven days before its occurrence which includes three M∼4 earthquakes. There have never been a $M \geq 5$ earthquake rupturing Zone 2 over the past two decades (Shi et al., 2021). Earthquakes spread out the whole crust in the segment from shallow to deep (2 to 8 km). Roland et al. (2012) shows a wide damage zone (∼6 km perpendicular to the strike direction) across Zone 2 extending through the oceanic crust and penetrating into the upper-most mantle with a ∼10–20% P-wave velocity reduction. Such a damage zone differs strikingly from the fault zone structures of fully coupled mainshock zones, e.g., Zone 3 (Froment et al., 2014). The significant velocity reduction is most likely caused by enhanced seawater infiltration with fluid-filled porosity up to 8% (Roland et al., 2012; Froment et al., 2014). These characteristics suggest that the fault segment has pervasive fluid pathways and is embedded with small asperities that could only have $M < 5$ earthquakes. The Zone 2 fault segment likely slips aseismically to accommodate the plate deformation (Fig. 10; McGuire et al., 2012; Wolfson-Schwehr & Boettcher, 2019).

The Zone 2 fault segment likely participated in both initiating and terminating the 2008 M6 earthquake, therefore, it is denoted as the barrier zone of G3 (McGuire et al., 2012). Given the damaged zone is filled with fluid with an abundant supply, the large porosity values would lead to a strong dilatancy effect, which strengthening may have effectively stabilized the eastward rupture of the M6 earthquake (Y. Liu et al., 2020). Moreover, such dilatancy strengthening effects may also result in generating aseismic transients episodically, which may have accelerated the mainshock fault patch and led to the eventual rupture (Y. Liu et al., 2020). This model predicts seismic swarms driven by aseismic slip transients in Zone 2, and we observe a few swarm-like microseismicity sequences in the region that might reflect such transient slips (Fig. 5). The dilatancy effects enable the barrier zone to act as a "double agent" in nucleating and stopping earthquake ruptures in the adjacent locked zone.

The halt of crustal seismicity in Zone 2 after the M6 mainshock is perplexing. As predicted by the dilatancy model, the M6 mainshock would promote aseismic slips in the barrier zone, which would cause microseismicity in the region (Y. Liu et al., 2020). Additionally, static Coulomb stresses due to the M6 mainshock would increase in Zone 2, which should also encourage microseismicity (Fig. S10). If dilatency has played a role in the seismicity shutdown, its effects in porosity increase (pore-pressure drop) must be greater that those from the dilatancy-induced aseismic slips or Coulomb stress changes such that the effective normal stress increase from the pore-pressure drop provides a stronger clamping effects in reducing microeathquake activity in the barrier zone. Another possibility is that the accumulated strains in the barrier zone was temporarily depleted after the M6 mainshock, which would naturally cause a lack of seismicity in the barrier zone. Such a scenario is similar to the "asperity model" proposed in Aki (1984) that the mainshock patches are persistent asperities and the barrier zone slips smoothly during interseismic periods. In this case, limited strain would have accumulated in the barrier zone during the interseismic period. The dilatancy-induced clamping and the stress depletion could have both contributed to halting the seismicity after the M6 earthquake.

The boundaries between Zone 2 and Zone 1 and 3 are remarkably sharp as suggested by the seismicity shutdown after the M6 mainshock (Fig. 5), which is different from continental transform faults. For example, the creeping and locked sections of the central San Andreas Fault are connected by a $\sim$20 km transition zone with its seismicity rate tapering towards the locked section (Y. K. Liu et al., 2022). The sharp boundaries of Zone 2 could represent geometric complexities as a bend of seismicity trend in between Zone 2 and 3 is observed in our relocation catalog and in Froment et al. (2014). This transitional bend situates in the deep valley (Fig. 1), which suggests a local strike-normal extension (Pockalny et al., 1996; Gregg et al., 2006). Therefore, the barrier zone may have geometrically confined fault strands that connect to two locked zones. The geometric complexities might not have played as important a role as dilatency effects in limiting the M6 mainshock ruptures, but their spatial confinement may relate to the sharp boundaries of microseismicity in the barrier zone. Future investigations of seafloor morphology using high-resolution bathymetry data would shed new insights into the fault architecture of the barrier zone.

The fault zone materials of the barrier zone are likely significantly different from those of the locked zones (McGuire et al., 2012; Roland et al., 2012; Froment et al., 2014; Guo et al., 2018). Such along-strike variations in the fault zone structures have been observed at other OTFs (Searle, 1986; Whitmarsh & Calvert, 1986; Pockalny et al., 1996; Maia, 2019; Grevemeyer et al., 2021; Ren et al., 2022). The material variations at different Gofar segments likely associate with hydrothermal circulations, and the onsets of developing such variations may have been subjected to secondary tectonic processes, such as magma intrusion, plate motion changes, and jump of ridge positions (Mammerickx & Sandwell, 1986; Pockalny et al., 1996; Tebbens & Cande, 1997; Maia et al., 2016; Grevemeyer et al., 2021). These processes can couple with enhanced seawater infiltration, forming a positive feedback to promote developing damage zones (e.g,. Zone 2). The internal fault structure of Zone 2 shares some similarity with that of Zone 4, and the barrier zone may represent a more evolved stage of Zone 4 with a higher degree of fractures.

5.1.3 Ridge and Transform Fault Interactions

Most of the earthquakes in Zone 5 occurred in the crust with some nearly extending to the seafloor (Fig. 8). No M6 earthquake has ruptured this fault segment for the past two decade (Shi et al., 2021). The widespread seismicity and the lack of M6 earthquakes suggest that Zone 5 is also a damage zone and can potentially serve as a barrier zone to influence seismicity in Zone 4. Similar to Zone 2, this fault segment is likely fully saturated with seawater, and fluid may play a primary role in modulating earthquakes in Zone 5. Consequentially, dilatency effects are expected to be strong and aseismic slip may predominantly release the accumulated tectonic stress in the segment. However, the fault segment differs from Zone 2 in two major aspects: almost all earthquakes occurred in the crust and there were quasi-periodic earthquake swarms in Zone 5 throughout the 2008 experiment.

Spectral analysis of the daily seismicity rate indicates that the swarms in Zone 5 have a recurrence interval of $\sim$24.4 days (Fig. S11). Particularly, an intense swarm of 2,096 events occurred in December, lasting up to two-weeks. The December swarm likely initiated around 2008-12-06 11:00 AM UTC from the western end of the transform fault and migrated towards the east with an average propagation speed of 5.4 km per day (Fig. 9). This swarm includes two M5 earthquakes that occurred at 2008-12-07 08:53:22 UTC and 2008-12-07 14:15:31 UTC (Fig. S9). Most of the larger magnitude events occurred during the first two days of the swarm (Fig. 9), and several M$\geq$2 events also occurred in Zone 4 as part of the sequence (Fig. 9). The swarm broke a fault patch that was previously quiescent, resulting in 823 microearthquakes within a 2 km footprint for 12 days. We consider this December sequence as a swarm instead of a foreshock-mainshock-aftershock sequence because of the clear migration pattern and the seismicity rate pattern, no single dominant earthquake as an obvious mainshock.

The depth limit in earthquakes and the quasi-periodic swarms likely reflect influences from the spreading center. The Zone 5 segment is at the intersection between the ridge and transform fault, and the thermal structure will favor a shallow downdip edge of the seismogenic zone (Roland et al., 2010). Further, the periodic swarms might be related to magma/fluid activity or transient slip events. The swarm periodicity does not match the semidiurnal ocean tides that are known to trigger earthquakes at EPR (Stroup et al., 2007, 2009). The anomalistic month tide has a cycle of 27.5 days and it may not relate to the observed swarms since its period is longer than that of the Zone 5 swarms. Magma chamber activity can couple with tidal stresses to modulate seismicity of near-ridge faults (Scholz et al., 2019). Therefore, the swarms could be due to combined effects of magma activity and tidal stresses. Additionally, fluid pockets/pathways in fault zones may experience frequent recharge and discharge processes, leading to periodic fluid migrations in the fault zone fractures, which can also produce similar swarms at various spatiotemporal scales (Ross et al., 2020; Ross & Cochran, 2021). There was a temporary pause of the periodic swarms soon after the M6 mainshock (Fig. 8). We speculate that the pause might relate to triggered aseismic slips in Zone 5 by the M6 mainshock. The triggered aseismic slips would promote a temporary porosity increase and cause a pore-pressure decrease (Y. Liu et al., 2020). Such a process would clamp the fault (dilatency effects) and discourage microearthquakes. The pore-pressure drop eventually recovered as suggested by the seismicity (Fig. 8), which may have been assisted by intense hydrothermal circulation in the damaged fault zone due to close proximity to the ridge. If this scenario holds true, fluid migration and hydrothermal circulation may be the primary cause of the Zone 5 swarms.

The fault patch of Group 2 earthquakes in Zone 5 likely represents a different fault strand than that had the M5 doublet and the rest of the December swarm (Group 1). The fault strand may have been surrounded by barriers that were broken by the M5 earthquakes, and the influx of fluid may have caused the intense swarm. Such a hypothesis is supported by the lack of earthquake similarities between the two groups in Zone 5 and the absence of events prior to the December swarm. The current bathymetry data cannot distinguish possible seafloor morphological features related to the fault strand of the Group 2 earthquakes, but the ridge-transform connection likely produce a complex, heterogenous fault network, such as indicated by the prominent "J"-shape structure of EPR.

5.2 Deep Earthquakes, Fluid-Rock Interaction, and Upper-Mantle Thermal Structure

Depth extent of microseismicity decreases from east to west along the westernmost Gofar transform fault as indicated by the 95 percentile seismicity depth of its five segments (Fig. 3). The nominal depth extent of OTF seismicity is primarily controlled by the position of the 600°C isotherm (Bergman & Solomon, 1988; Abercrombie & EkstroÈm, 2001; Boettcher et al., 2007; Behn et al., 2007; Braunmiller & Nábělek, 2008; Roland et al., 2010). At Gofar, the 600°C isotherm is likely above or near the crust-mantle boundary at ∼7 km (Roland et al., 2010), which would create a narrow layer of aftershock near Moho that separates the locked layer in the crust from free creeping layer in the mantle, such as the events of Group 1 in Zone 3 (Fig. 6c and 10). Microearthquakes also occur in the upper-mantle at the eastern G3 (Zone 1 to 3) from 7 to 10 km, including Group 2 in Zone 1 (Fig. 4d), Group 2 and 3 in Zone 2 (Fig. 5d and e), and Group 2 and 3 in Zone 3 (Fig. 6d and e). These deep seismicity is consistent with previous earthquake location results albeit at shallower depths (McGuire et al., 2012; Guo et al., 2018). Comparing to EPR, the ITSC likely has less magma supply and lower temperature (Pickle et al., 2009). The deepening of the 95% seismicity depth contour could indicate an upper-mantle thermal structure with the 600°C isotherm deepening from west (EPR) to east (ITSC). However, such an isotherm transition would occur gradually over a large spatial extent in contrast to our observed staircase-changes (Fig. 3). Furthermore, an isotherm deepening alone cannot explain the depth gaps between two layers of seismicity in Zone 1, 2, and 3 (Fig. 4, 5, 6, and 10).

Fluid-rock interaction would also generate earthquakes below the expected 600°C isotherm (A. H. Kohli & Warren, 2020; Kuna et al., 2019; Yu et al., 2021). As the barrier zone (Zone 2) centers at the eastern section of G3, its fractures would lead to enhanced permeability within and around the segment, promote hydrothermal circulation to the upper mantle, and lower the ambient mantle temperature (A. H. Kohli & Warren, 2020). Such fluid-rock interactions would alter the minerals and promote seismicity in the upper mantle (Prigent et al., 2020). Further, fractures in the high temperature peridotite mylonites (≥800°C) and/or coarse-grained peridotite are capable to host brittle failures at ambient mantle temperature conditions (Fig. 10; Prigent et al., 2020; A. Kohli et al., 2021; Yu et al., 2021). For example, deep seismicity at the Romanche transform fault can occur down to 30 km depth, which would be in a temperature range of 700°C to 900°C (Yu et al., 2021). These two mechanisms are not exclusive, and they both enable strain to localize at deeper depth beyond the Moho discontinuity. Finally, fluid-rock interaction can couple with the upper-mantle thermal structure to promote deep seismicity in conjunction at G3 (Fig. 10).

The temporal behaviors of deep microseismicity vary from patch to patch, indicating that their physical drivers are likely dissimilar. For example, intermittent seismicity bursts are observed at Group 2 in Zone 1, Group 3 in Zone 2, and Group 3 of Zone 3 (Fig. 4d, 5e, and 6e). These bursts do not seem to be strongly influenced by the 2008 M6 mainshock. Most of the seismicity bursts are not mainshock-aftershock sequences. Therefore, they may be more likely related to episodic fluid activity or transient slips.

Similar two layers of seismicity are observed at the Blanco transform fault with the deep layer in the upper mantle at 13 km depth migrating as swarms, which were likely driven by creeps partially and episodically (Kuna et al., 2019). In contrast, the deep bursts at Gofar do no have clear migration patterns, suggesting that their driving forces are likely local. Another class of deep seismicity occurred continuously throughout the year and their temporal behaviors correlate the M6 mainshock. For example, Group 2 in Zone 2 suddenly paused after the mainshock (Fig. 5d), similar to the shallow seismicity in the barrier zone, indicating possible connections (Fig. 10). Earthquakes of Group 2 in Zone 3 also correlate with the M6 mainshock with an apparent increase in seismicity after the M6 mainshock, which might have been affected by its afterslip (Fig. 6d).

5.3 Fault Interaction

Different Gofar fault segments actively interact with each other and yield correlated seismic activities. For example, the barrier zone may have regulated the M6 mainshock in both its rupture nucleation and termination (Fig. 5). The M6 mainshock paused seismicity in the barrier zone (Fig. 5) and disturbed the quasi-periodic swarms in the Zone 5 (Fig. 8). Seismicity in Zone 4 is influenced by both the M6 mainshock and the December swarm (Fig. 7). These interactions likely involve multiple concurrent physical processes that may facilitate each other to fabricate the observed complex seismicity evolution at Gofar. For example, stress triggering due to the dynamic and/or static stress changes could cause aseismic slips or transients, which may interact with the fluid-driven seismicity at various fault patches (Shelly et al., 2011; van der Elst et al., 2013; Kaven, 2020; Ross et al., 2020). We infer that complex architecture, material property variation, and intense seawater infiltration would cause stress heterogeneity and stimulate prevalent aseismic slips. Such aseismic slips could propagate over a large range episodically, bridging along-strike and along-dip fault interactions. The highly heterogeneous stress field is sensitive to perturbations either from transients or fluid migrations. The complex fault architecture and material variation produce geometric and mechanical segmentation, which are represented as the complex seismicity evolution.

6 Conclusions

We detect, locate, and relocate 30,854 earthquakes at the westernmost Gofar transform fault using a one-year OBS data collected in 2008. The microearthquakes have complex spatiotemporal patterns, suggesting distinct five segments of the transform fault along strike. We find that

1. Two locked fault patches that can have characteristic M6 earthquakes are distributed within the oceanic crust with their down-dip edges marked by microearthquakes.
2. Two damage zones have microearthquakes spreading out the whole oceanic crust.
3. The locked fault segments have simple fault geometries while the damage zones are likely comprised of multiple strands.
4. Episodic seismicity bursts frequently occur in Zone 5 that connects the transform fault to the East Pacifc Rise.
5. Deep seismicity in the upper mantle is observed at the eastern section of the transform fault up to 10 km, often as intermittent seismicity bursts.

Taking microseismicity as a proxy of the fault slip modes, we infer that

1. The primary slip mode varies from segment to segment, but the seismic and aseismic slip modes are not exclusive in the same segment, particularly at the along-dip direction.
2. Complex fault architecture likely contributes to the observed segmentation.

3. The damage zones are likely pervasively fractured with enhanced seawater infiltration.
4. Fluid-rock interaction is crucial in controlling slip events in the damage zone and in modulating earthquake ruptures in locked zones.
5. Multiple physical processes may concur and cause the fault segments interact with each other, producing the complex seismicity pattern.

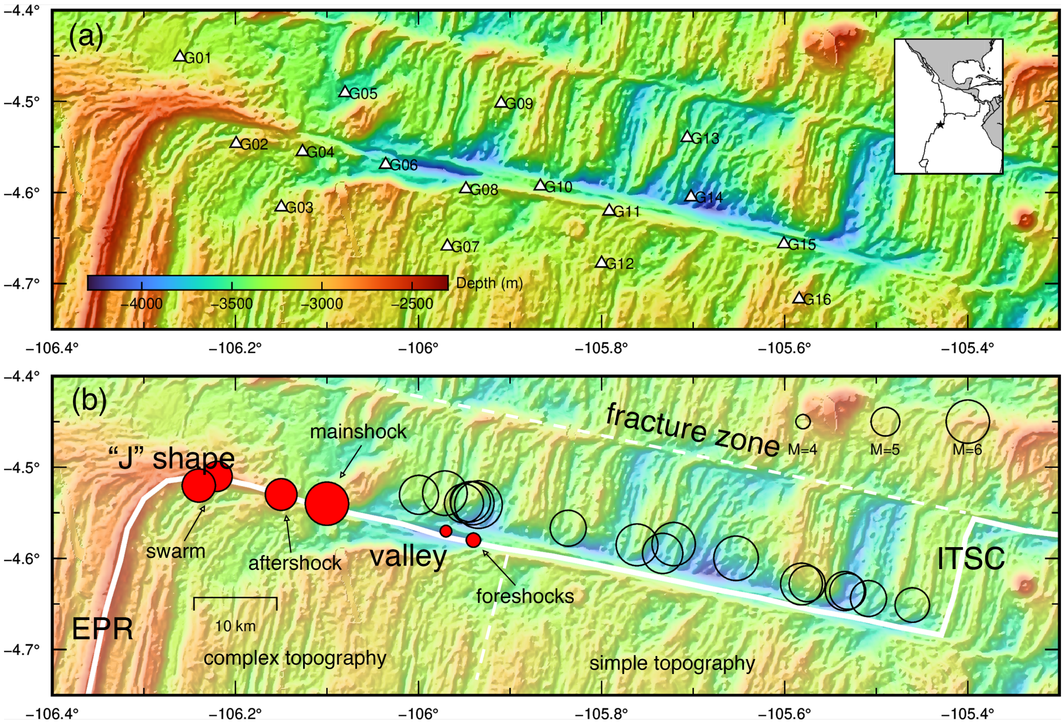

Figure 1. Bathymetry and structural interpretation of the westernmost Gofar transform fault. (a) Bathymetry of study area. White labelled triangles are OBS stations. Inset shows location of study area at East Pacific Rise. (b) Structural interpretation of study area. Solid white line marks the trace of ridges and transform fault. White dash line denotes fracture zone. "J"-shape structure and deep valley are denoted on the map. Red solid circles are the epicenters of the 2008 M6 mainshock, its largest aftershock, two M5 events during December swarm, and three M4 events in the barrier zone. Black open circles are M≥5 earthquake locations from Shi et al. (2021). EPR stands for East Pacific Rise. ITSC stands for intra-transform spreading center.

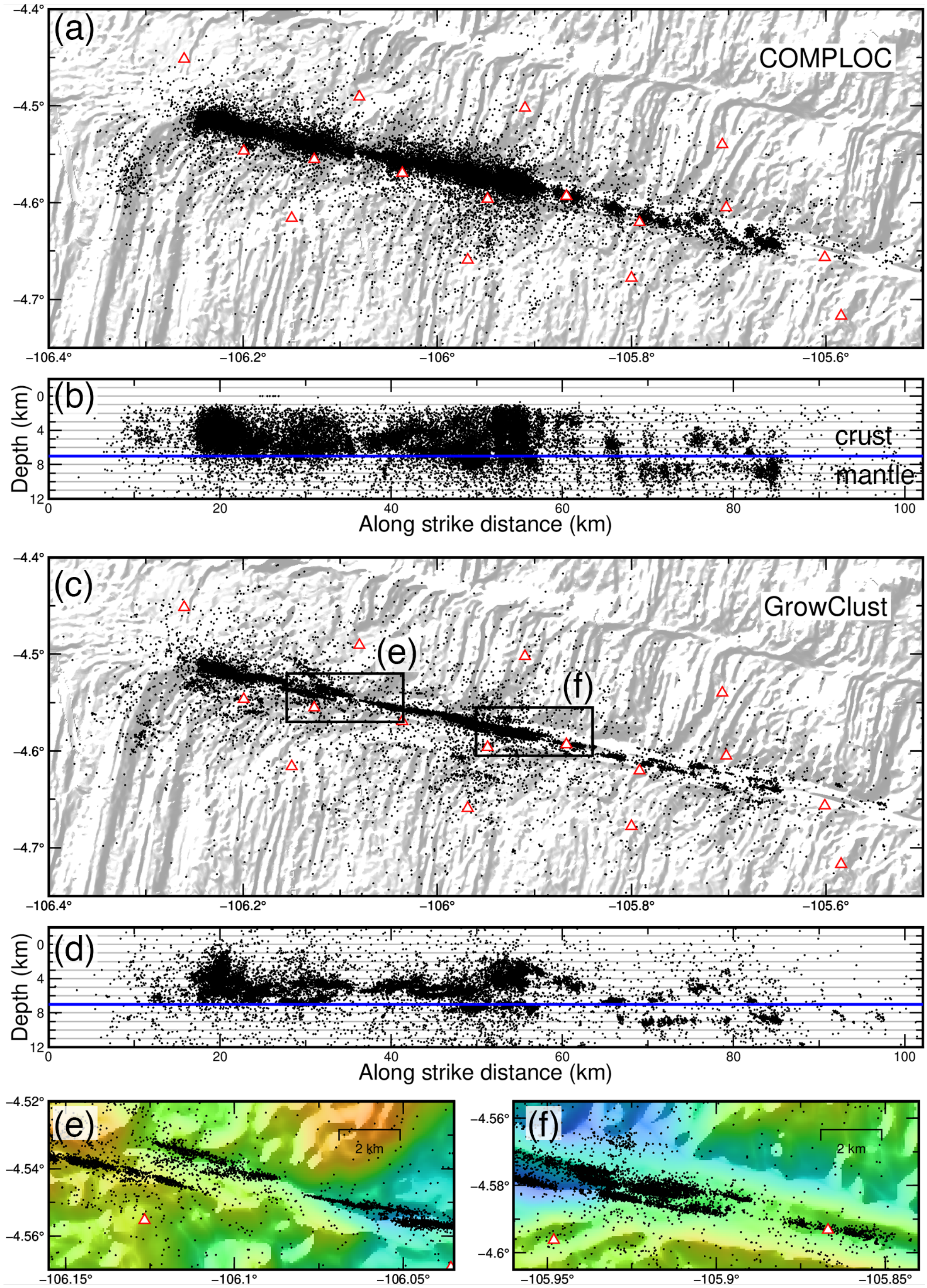

Figure 2. Earthquake location and relocation results. (a) and (b) Map and depth views of COMPLOC earthquake locations. (c) and (d) Map and depth views of GrowClust earthquake relocations. Blue lines mark the 7 km depth, which we infer as the local Moho discontinuity. (e) and (f) Zoom-in views of two rectangular areas in (c). Background color denotes seafloor bathymetry using the same color scale as in Fig. 1. White open triangles are OBS stations.

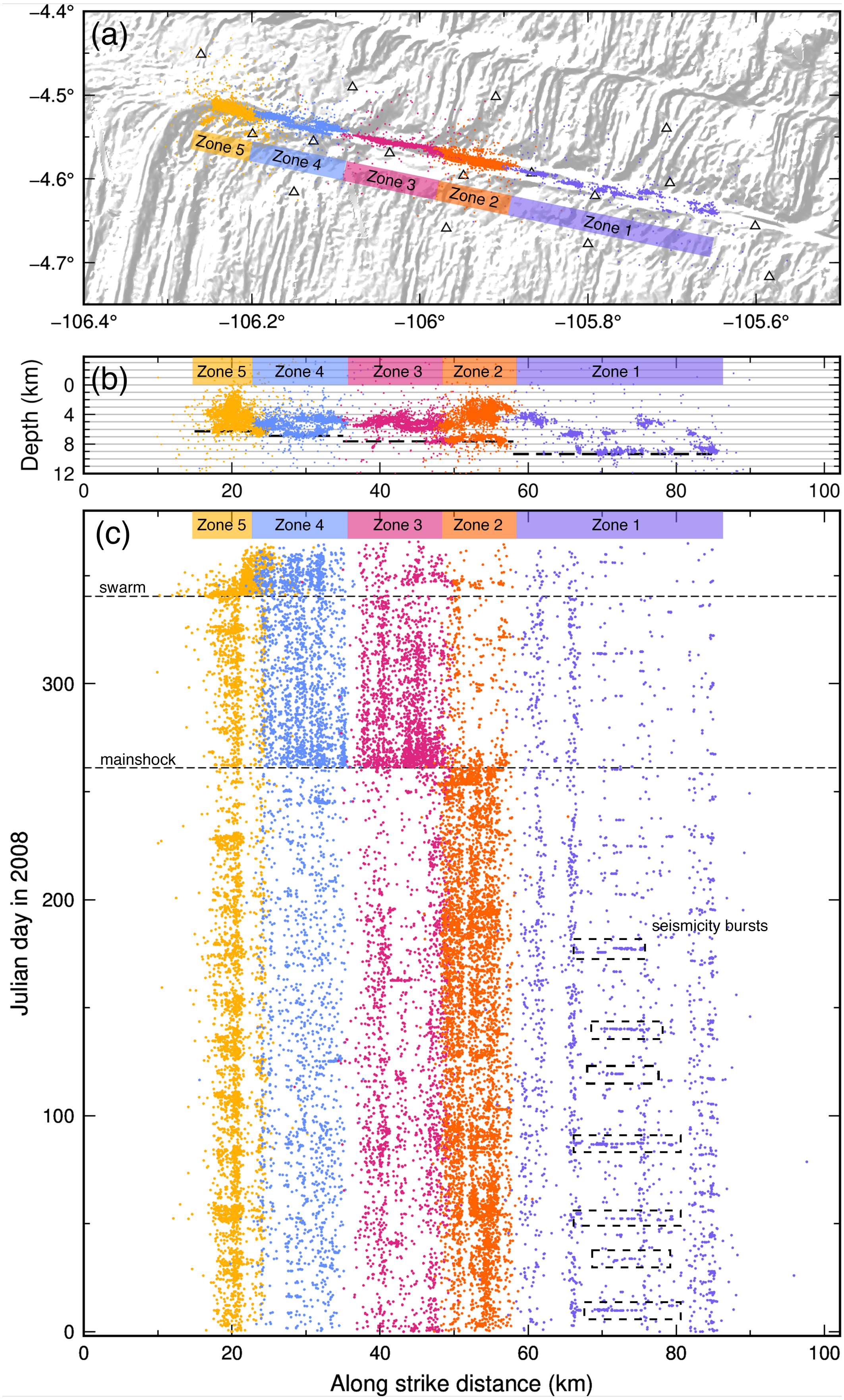

Figure 3. Spatiotemporal evolution of Gofar G3 microearthquakes. (a) and (b) Map and depth views of earthquakes in the five fault zones. Black dash lines in (b) denote 95% earthquake depth extents of each zone. (c) Spatiotemporal evolution of earthquakes in the five zones. The occurrence times of the M6 mainshock and the December swarm are denoted by black dash lines. Example seismicity bursts in Zone 1 are highlighted by dash-line rectangles.

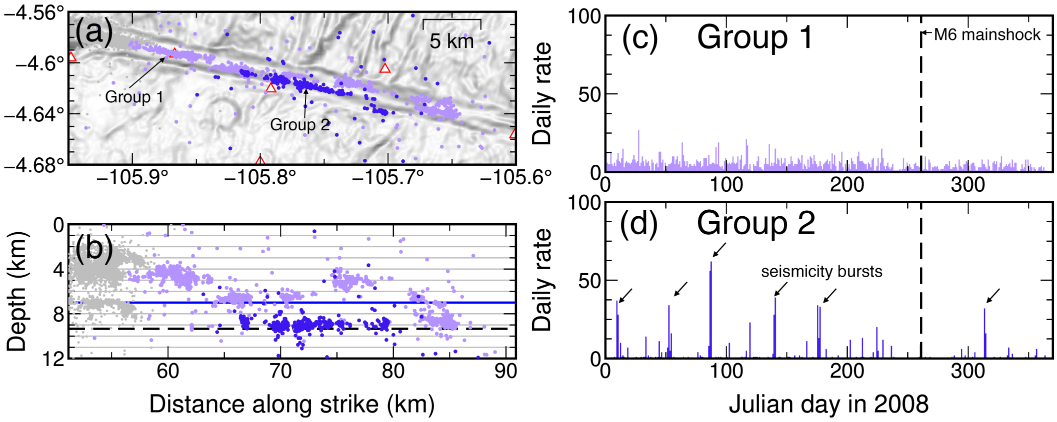

Figure 4. Earthquakes in Zone 1. (a) and (b) Map and depth views of earthquakes in Zone 1. Different colors indicate two groups of the earthquakes. Blue line in (b) denotes 7 km depth and black dash line denotes 95% seismicity depth, 9.3 km. (c) and (d) Temporal evolution of earthquakes in Group 1 and 2 of Zone 1. Seismicity bursts are marked with black arrows. Black dash line in (c–d) denotes the occurrence time of the M6 mainshock.

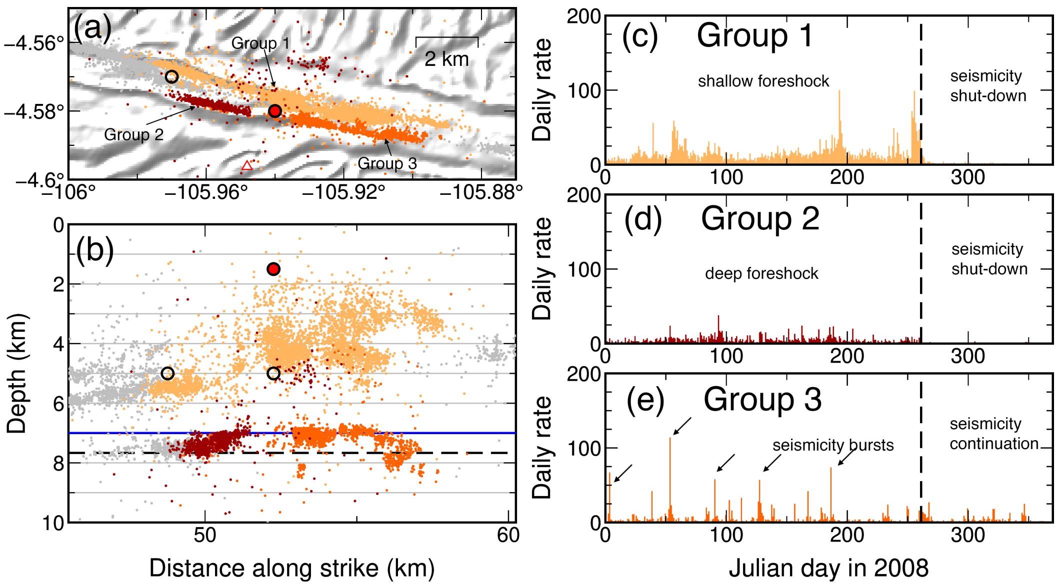

Figure 5. Earthquakes in Zone 2. (a) and (b) Map and depth views of earthquakes in Zone 2. Different colors indicate different groups of the earthquakes. Red solid circles (depth resolved) and black open circles (depth assigned as 5 km) in (b) denote three M∼4 events during the 7-day foreshock sequence preceding the M6 mainshock. Blue line in (b) denotes 7 km depth and black dash line denotes 95% seismicity depth, 7.7 km. (c) to (e) Temporal evolution of earthquakes in the three groups. Seismicity bursts in Group 3 are marked with black arrows. Black dash line in (c–e) denotes the occurrence time of the M6 mainshock.

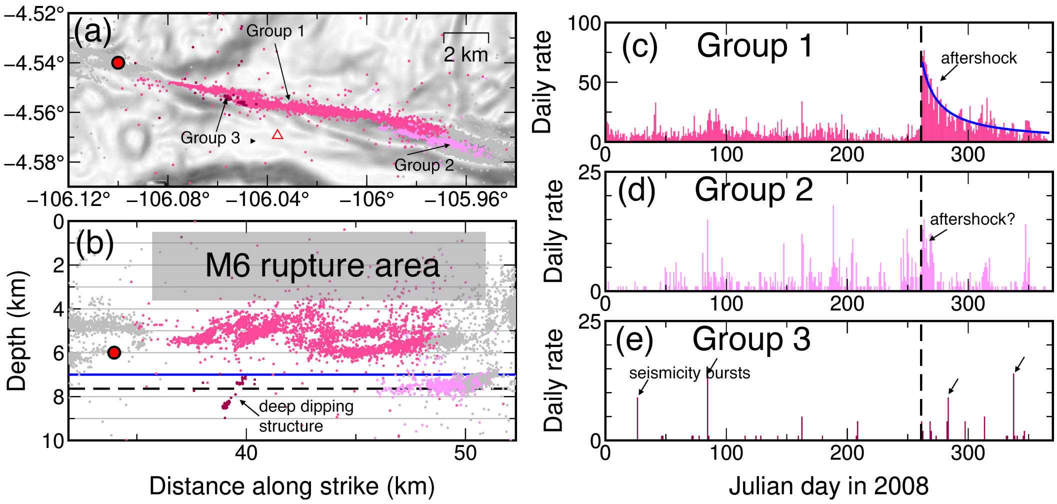

Figure 6. Earthquakes in Zone 3. (a) and (b) Map and depth views of earthquakes in Zone 3. Different colors indicate different groups of the earthquakes. Red solid circle (depth resolved) in (b) denotes the hypocenter of the M6 mainshock. Grey rectangular denotes the inferred rupture area of the mainshock. Blue line in (b) denotes 7 km depth and black dash line denotes 95% seismicity depth, 7.6 km. (c) to (e) Temporal evolution of earthquakes in the three groups. Aftershocks and seismicity bursts are marked with black arrows in (c–e). Aftershocks in Group 1 follow a t^{-1} Omori decay pattern as shown in (c). Black dash line in (c–e) denotes the occurrence time of the M6 mainshock.

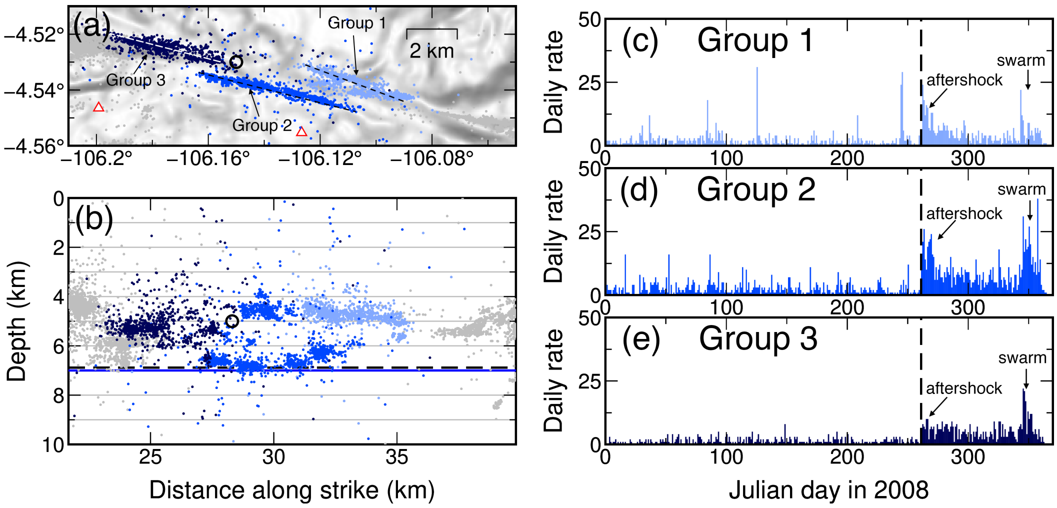

Figure 7. Earthquakes in Zone 4. (a) and (b) Map and depth views of earthquakes in Zone 4. Different colors indicate different groups of the earthquakes. Dash lines in (a) indicate inferred fault traces associated with the three earthquake groups of Zone 4. Black open circle in (b) denotes the hypocenter of the M5 aftershock, which depth is assigned at 5 km. Blue line in (b) denotes 7 km depth and black dash line denotes 95% seismicity depth, 6.9 km. (c) to (e) Temporal evolution of earthquakes in the three groups. Aftershocks and events triggered by the December swarm are marked with black arrows in (c–e). Black dash line in (c–e) denotes the occurrence time of the M6 mainshock.

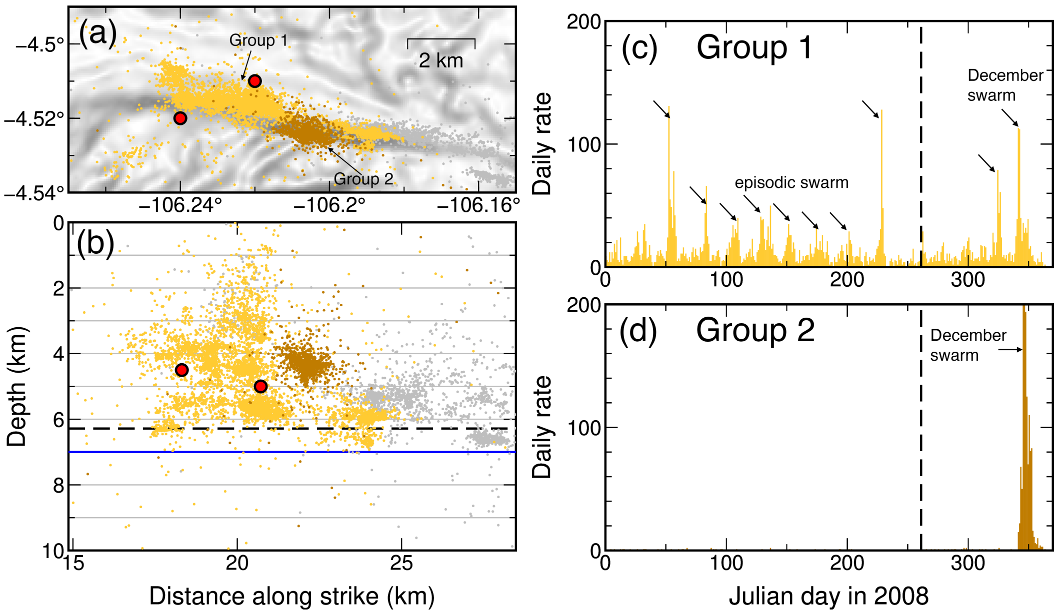

Figure 8. Earthquakes in Zone 5. (a) and (b) Map and depth views of earthquakes in Zone 5. Different colors indicate different groups of the earthquakes. Red solid circles (depth resolved) in (b) denote the hypocenters of the two M5 events during the December swarm. Blue line in (b) denotes 7 km depth and black dash line denotes 95% seismicity depth, 6.3 km. (c) and (d) Temporal evolution of earthquakes in the three groups. Swarm events are marked with black arrows in (c–d). Black dash lines in (c–d) denote the occurrence time of the M6 mainshock.

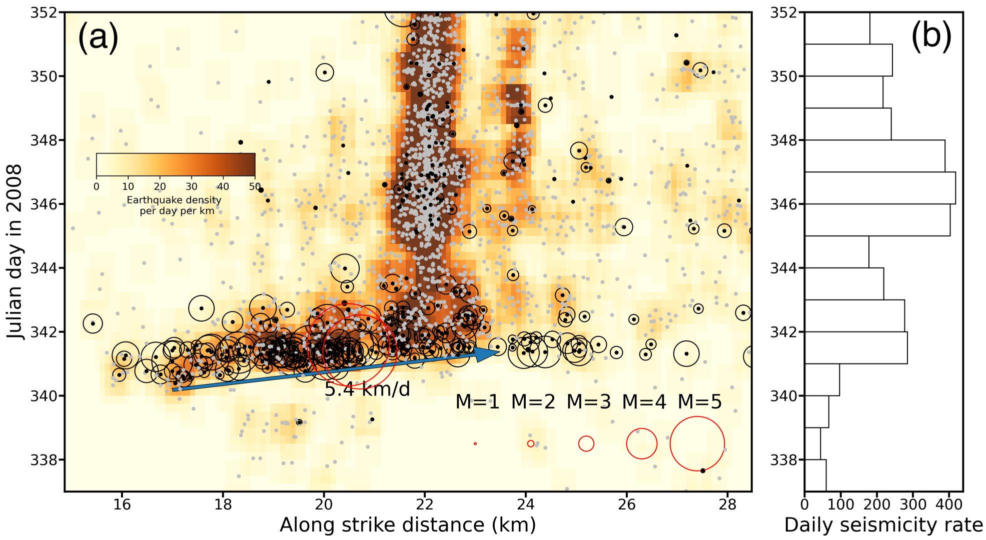

Figure 9. December swarm in Zone 5. (a) Spatiotemporal evolution of the December swarm. Background color denotes earthquake density ($\mathrm{km}^{-1} \cdot \mathrm{day}^{-1}$). Gray dots denote earthquakes without magnitude estimates. Black dots denote earthquakes having magnitude estimates with their open circle radii showing the earthquake magnitudes. Blue arrow denotes the inferred migration direction of the swarm. (b) Daily seismicity rate of the December swarm in Zone 5.

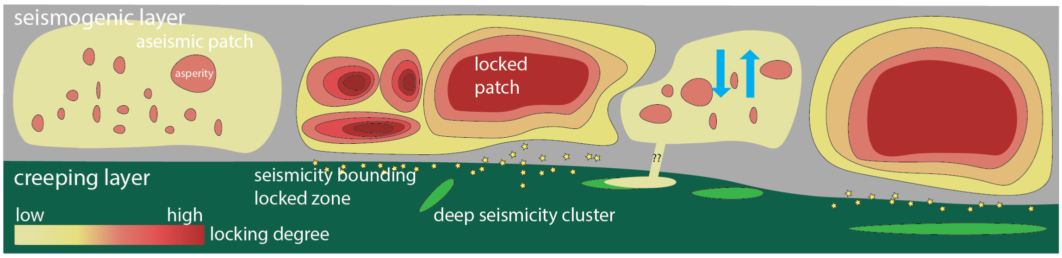

Figure 10. Conceptual model of microseismicity and fault slip modes of the westernmost Gofar transform fault. Irregular shaped patches denote fault patches of various sizes, and their colors correspond to different locking degrees. Zone 1, 3 and 4 are represented as sporadic, locked patches. Zone 2 and 5 are represented as damage zones embedded with small asperities. Microseismicity near the Moho discontinuity are denoted as small yellow stars. Green and yellow ellipses denote deep seismicity clusters. Blue arrows denote intense fluid circulation in Zone 2.

Open Research

The seismic data are available from the Data Management Center (DMC) of the Incorporated Research Institutions for Seismology (IRIS) under the network codes ZD. IRIS Data Services, and the IRIS Data Management Center, were used to access waveforms, related metadata, and derived products used in this study. IRIS Data Services are funded through the Seismological Facilities for the Advancement of Geoscience and EarthScope (SAGE) Proposal of the National Science Foundation (NSF) under Cooperative Agreement EAR-1261681. The earthquake catalog was downloaded from the International Seismological Center (ISC) and the bathymetry data can be obtained from `https://www.ngdc.noaa.gov/maps/autogrid/`. We used open-source software EQTransformer (Mousavi et al., 2020), REAL (Zhang et al., 2019), COMPLOC (G. Lin & Shearer, 2006) and GrowClust (Trugman & Shearer, 2017) for earthquake detection, association, location and relocation. The earthquake catalog will be included in the supplementary material upon publication of the study.

Acknowledgments

J.G and W.F acknowledge support from National Science Foundation (NSF) grant OCE-1833279 and EAR-2143413. The ocean bottom seismometer instruments were provided by the Ocean Bottom Seismograph Instrument Center (OBSIP). The authors thank Jeffrey McGuire, John Collins, and the rest of the 2008 Quebrada-Discovery-Gofar experiment team for collecting and archiving the data. The authors thank Peter Shearer for teaching us the COMPLOC and GrowClust software, and Yajing Liu, Mark Behn, and Chen Ji for insightful discussions.

References

Abercrombie, R. E., & EkstroÈm, G. (2001). Earthquake slip on oceanic transform faults. *Nature*, *410*(6824), 74–77.

Aderhold, K., & Abercrombie, R. E. (2016). The 2015 Mw 7.1 earthquake on the Charlie-Gibbs transform fault: Repeating earthquakes and multimodal slip on a slow oceanic transform. *Geophysical Research Letters*, *43*(12), 6119-6128. doi: https://doi.org/10.1002/2016GL068802

Aki, K. (1965). Maximum likelihood estimate of b in the formula log n= a-bm and its confidence limits. *Bull. Earthq. Res. Inst., Tokyo Univ.*, *43*, 237–239.

Aki, K. (1984). Asperities, barriers, characteristic earthquakes and strong motion prediction. *Journal of Geophysical Research: Solid Earth*, *89*(B7), 5867–5872.

Allen, R. V. (1978). Automatic earthquake recognition and timing from single traces. *Bulletin of the Seismological Society of America*, *68*(5), 1521-1532. doi: 10.1785/BSSA0680051521

Avouac, J.-P. (2015). From geodetic imaging of seismic and aseismic fault slip to dynamic modeling of the seismic cycle. *Annual Review of Earth and Planetary Sciences*, *43*(1), 233-271. doi: 10.1146/annurev-earth-060614-105302

Bakun, W. H., Aagaard, B., Dost, B., Ellsworth, W. L., Hardebeck, J. L., Harris, R. A., . . . Waldhauser, F. (2005). Implications for prediction and hazard assessment from the 2004 Parkfield earthquake. *Nature*, *437*(7061), 969-974. doi: 10.1038/nature04067

Barka, A. A., & Kadinsky-Cade, K. (1988). Strike-slip fault geometry in Turkey and its influence on earthquake activity. *Tectonics*, *7*(3), 663-684. doi: https://doi.org/10.1029/TC007i003p00663

Behn, M. D., Boettcher, M. S., & Hirth, G. (2007). Thermal structure of oceanic transform faults. *Geology*, *35*(4), 307–310.

Bergman, E. A., & Solomon, S. C. (1988). Transform fault earthquakes in the north atlantic: Source mechanisms and depth of faulting. *Journal of Geophysical Research: Solid Earth*, *93*(B8), 9027–9057.

Boettcher, M. S., Hirth, G., & Evans, B. (2007). Olivine friction at the base of oceanic seismogenic zones. *Journal of Geophysical Research: Solid Earth*, *112*(B1).

Boettcher, M. S., & Jordan, T. H. (2004). Earthquake scaling relations for mid-ocean ridge transform faults. *Journal of Geophysical Research: Solid Earth*, *109*(B12). doi: https://doi.org/10.1029/2004JB003110

Braunmiller, J., & Nábělek, J. (2008). Segmentation of the Blanco Transform Fault Zone from earthquake analysis: Complex tectonics of an oceanic transform fault. *Journal of Geophysical Research: Solid Earth*, *113*(B7). doi: https://doi.org/10.1029/2007JB005213

Brocher, T. M., Baltay, A. S., Hardebeck, J. L., Pollitz, F. F., Murray, J. R., Llenos, A. L., ... Scharer, K. M. (2015, 02). The Mw 6.0 24 August 2014 South Napa Earthquake. *Seismological Research Letters*, *86*(2A), 309-326. doi: 10.1785/0220150004

Castellanos, J. C., Zhan, Z., & Wu, W. (2020). Absolute centroid location of submarine earthquakes from 3D waveform modeling of water reverberations. *Journal of Geophysical Research: Solid Earth*, *125*(5), e2019JB018941.

Chan, C.-H., & Stein, R. S. (2009). Stress evolution following the 1999 Chi-Chi, Taiwan, earthquake: Consequences for afterslip, relaxation, aftershocks and departures from Omori decay. *Geophysical Journal International*, *177*(1), 179-192. doi: 10.1111/j.1365-246X.2008.04069.x

Freed, A. M. (2005). Earthquake triggering by static, dynamic, and postseismic stress transfer. *Annual Review of Earth and Planetary Sciences*, *33*(1), 335-367. doi: 10.1146/annurev.earth.33.092203.122505

Froment, B., McGuire, J. J., van der Hilst, R. D., Gouédard, P., Roland, E. C., Zhang, H., & Collins, J. A. (2014). Imaging along-strike variations in mechanical properties of the Gofar transform fault, East Pacific Rise. *Journal of Geophysical Research: Solid Earth*, *119*(9), 7175-7194. doi: https://doi.org/10.1002/2014JB011270

Gong, J., Fan, W., & Parnell-Turner, R. (2022). Microseismicity indicates atypical small-scale plate rotation at the Quebrada transform fault system, East Pacific Rise. *Geophysical Research Letters*, *49*(3), e2021GL097000. doi: https://doi.org/10.1029/2021GL097000

Gregg, P. M., Lin, J., & Smith, D. K. (2006). Segmentation of transform systems on the east pacific rise: Implications for earthquake processes at fast-slipping oceanic transform faults. *Geology*, *34*(4), 289–292.

Grevemeyer, I., Rüpke, L. H., Morgan, J. P., Iyer, K., & Devey, C. W. (2021). Extensional tectonics and two-stage crustal accretion at oceanic transform faults. *Nature*, *591*(7850), 402-407. doi: 10.1038/s41586-021-03278-9

Guo, H., Zhang, H., & Froment, B. (2018). Structural control on earthquake behaviors revealed by high-resolution Vp/Vs imaging along the Gofar transform fault, East Pacific Rise. *Earth and Planetary Science Letters*, *499*, 243-255. doi: https://doi.org/10.1016/j.epsl.2018.07.037

Han, S., Bangs, N. L., Carbotte, S. M., Saffer, D. M., & Gibson, J. C. (2017, Dec 01). Links between sediment consolidation and Cascadia megathrust slip behaviour. *Nature Geoscience*, *10*(12), 954-959. doi: 10.1038/s41561-017-0007-2

Hardebeck, J. L., Nazareth, J. J., & Hauksson, E. (1998). The static stress change triggering model: Constraints from two southern California aftershock sequences. *Journal of Geophysical Research: Solid Earth*, *103*(B10), 24427–24437.

Harris, R. A. (2017). Large earthquakes and creeping faults. *Reviews of Geophysics*, *55*(1), 169-198. doi: https://doi.org/10.1002/2016RG000539

Harris, R. A., & Day, S. M. (1999). Dynamic 3D simulations of earthquakes on En Echelon Faults. *Geophysical Research Letters*, *26*(14), 2089-2092. doi: https://

doi.org/10.1029/1999GL900377

Hicks, S. P., Okuwaki, R., Steinberg, A., Rychert, C. A., Harmon, N., Abercrombie, R. E., … Sudhaus, H. (2020, 01). Back-propagating supershear rupture in the 2016 Mw 7.1 Romanche transform fault earthquake. *Nature Geoscience*, *13*(9), 647-653.

Hsu, Y.-J., Simons, M., Avouac, J.-P., Galetzka, J., Sieh, K., Chlieh, M., … Bock, Y. (2006). Frictional afterslip following the 2005 Nias-Simeulue earthquake, Sumatra. *Science*, *312*(5782), 1921-1926. doi: 10.1126/science.1126960

Jiang, J., Bock, Y., & Klein, E. (2021). Coevolving early afterslip and aftershock signatures of a San Andreas fault rupture. *Science Advances*, *7*(15), eabc1606. doi: 10.1126/sciadv.abc1606

Kato, A., Obara, K., Igarashi, T., Tsuruoka, H., Nakagawa, S., & Hirata, N. (2012). Propagation of slow slip leading up to the 2011 M w 9.0 Tohoku-Oki earthquake. *Science*, *335*(6069), 705–708.

Kaven, J. O. (2020). Seismicity rate change at the Coso geothermal field following the July 2019 Ridgecrest earthquakes. *Bulletin of the Seismological Society of America*, *110*(4), 1728-1735. doi: 10.1785/0120200017

King, G. C. P., Stein, R. S., & Lin, J. (1994). Static stress changes and the triggering of earthquakes. *Bulletin of the Seismological Society of America*, *84*(3), 935-953. doi: 10.1785/BSSA0840030935

Kohli, A., Wolfson-Schwehr, M., Prigent, C., & Warren, J. M. (2021). Oceanic transform fault seismicity and slip mode influenced by seawater infiltration. *Nature Geoscience*, *14*(8), 606-611. doi: 10.1038/s41561-021-00778-1

Kohli, A. H., & Warren, J. M. (2020). Evidence for a deep hydrologic cycle on oceanic transform faults. *Journal of Geophysical Research: Solid Earth*, *125*(2), e2019JB017751. doi: https://doi.org/10.1029/2019JB017751

Kuna, V. M., Nábělek, J. L., & Braunmiller, J. (2019). Mode of slip and crust–mantle interaction at oceanic transform faults. *Nature Geoscience*, *12*(2), 138-142. doi: 10.1038/s41561-018-0287-1

Lay, T., Kanamori, H., Ammon, C. J., Koper, K. D., Hutko, A. R., Ye, L., … Rushing, T. M. (2012). Depth-varying rupture properties of subduction zone megathrust faults. *Journal of Geophysical Research: Solid Earth*, *117*(B4). doi: 10.1029/2011JB009133

Lin, G., & Shearer, P. (2005). Tests of relative earthquake location techniques using synthetic data. *Journal of Geophysical Research: Solid Earth*, *110*(B4). doi: https://doi.org/10.1029/2004JB003380

Lin, G., & Shearer, P. (2006). The COMPLOC earthquake location package. *Seismological Research Letters*, *77*(4), 440-444.

Lin, J., & Stein, R. S. (2004). Stress triggering in thrust and subduction earthquakes and stress interaction between the southern San Andreas and nearby thrust and strike-slip faults. *Journal of Geophysical Research: Solid Earth*, *109*(B2). doi: https://doi.org/10.1029/2003JB002607

Liu, Y., McGuire, J. J., & Behn, M. D. (2012). Frictional behavior of oceanic transform faults and its influence on earthquake characteristics. *Journal of Geophysical Research: Solid Earth*, *117*(B4).

Liu, Y., McGuire, J. J., & Behn, M. D. (2020). Aseismic transient slip on the Gofar transform fault, East Pacific Rise. *Proceedings of the National Academy of Sciences*, *117*(19), 10188–10194. doi: 10.1073/pnas.1913625117

Liu, Y., & Rice, J. R. (2005). Aseismic slip transients emerge spontaneously in three-dimensional rate and state modeling of subduction earthquake sequences. *Journal of Geophysical Research: Solid Earth*, *110*(B8). doi: https://doi.org/10.1029/2004JB003424

Liu, Y. K., Ross, Z. E., Cochran, E. S., & Lapusta, N. (2022). A unified perspective of seismicity and fault coupling along the San Andreas Fault. *Science Advances*, *8*(8), eabk1167. doi: 10.1126/sciadv.abk1167

Maeda, N. (1985). A method for reading and checking phase times in autoprocessing system of seismic wave data. *Zisin*, *38*, 365-379.

Maia, M. (2019). Chapter 3 - Topographic and Morphologic Evidences of Deformation at Oceanic Transform Faults: Far-Field and Local-Field Stresses. In J. C. Duarte (Ed.), *Transform Plate Boundaries and Fracture Zones* (p. 61-87). Elsevier. doi: https://doi.org/10.1016/B978-0-12-812064-4.00003-7

Maia, M., Sichel, S., Briais, A., Brunelli, D., Ligi, M., Ferreira, N., ... Oliveira, P. (2016). Extreme mantle uplift and exhumation along a transpressive transform fault. *Nature Geoscience*, *9*(8), 619-623. doi: 10.1038/ngeo2759

Mammerickx, J., & Sandwell, D. (1986). Rifting of old oceanic lithosphere. *Journal of Geophysical Research: Solid Earth*, *91*(B2), 1975-1988. doi: https://doi.org/10.1029/JB091iB02p01975

Marone, C. J., Scholtz, C. H., & Bilham, R. (1991). On the mechanics of earthquake afterslip. *Journal of Geophysical Research: Solid Earth*, *96*(B5), 8441-8452. doi: https://doi.org/10.1029/91JB00275

McGuire, J. J. (2008). Seismic cycles and earthquake predictability on East Pacific Rise transform faults. *Bulletin of the Seismological Society of America*, *98*(3), 1067-1084. doi: 10.1785/0120070154

McGuire, J. J., Boettcher, M. S., & Jordan, T. H. (2005). Foreshock sequences and short-term earthquake predictability on East Pacific Rise transform faults. *Nature*, *434*(7032), 457-461. doi: 10.1038/nature03377

McGuire, J. J., Collins, J. A., Gouédard, P., Roland, E., Lizarralde, D., Boettcher, M. S., ... van der Hilst, R. D. (2012). Variations in earthquake rupture properties along the Gofar transform fault, East Pacific Rise. *Nature Geoscience*, *5*(5), 336-341. doi: 10.1038/ngeo1454

McLaskey, G. C. (2019). Earthquake initiation from laboratory observations and implications for foreshocks. *Journal of Geophysical Research: Solid Earth*, *124*(12), 12882-12904. doi: https://doi.org/10.1029/2019JB018363

Mousavi, S. M., Ellsworth, W. L., Zhu, W., Chuang, L. Y., & Beroza, G. C. (2020). Earthquake transformer—an attentive deep-learning model for simultaneous earthquake detection and phase picking. *Nature Communications*(1), 3952. doi: 10.1038/s41467-020-17591-w

Mousavi, S. M., Sheng, Y., Zhu, W., & Beroza, G. C. (2019). STanford EArthquake Dataset (STEAD): A global data set of seismic signals for AI. *IEEE Access*, *7*, 179464-179476. doi: 10.1109/ACCESS.2019.2947848

Moyer, P. A., Boettcher, M. S., McGuire, J. J., & Collins, J. A. (2018). Spatial and Temporal Variations in Earthquake Stress Drop on Gofar Transform Fault, East Pacific Rise: Implications for Fault Strength. *Journal of Geophysical Research: Solid Earth*, *123*(9), 7722-7740. doi: https://doi.org/10.1029/2018JB015942

Obara, K., & Kato, A. (2016). Connecting slow earthquakes to huge earthquakes. *Science*, *353*(6296), 253-257. doi: 10.1126/science.aaf1512

Pickle, R. C., Forsyth, D. W., Harmon, N., Nagle, A. N., & Saal, A. (2009). Thermo-mechanical control of axial topography of intra-transform spreading centers. *Earth and Planetary Science Letters*, *284*(3), 343-351. doi: https://doi.org/10.1016/j.epsl.2009.05.004

Pockalny, R. A., Gente, P., & Buck, R. (1996, 01). Oceanic transverse ridges: A flexural response to fracture-zone–normal extension. *Geology*, *24*(1), 71-74. doi: 10.1130/0091-7613(1996)024⟨0071:OTRAFR⟩2.3.CO;2

Prigent, C., Warren, J., Kohli, A., & Teyssier, C. (2020). Fracture-mediated deep seawater flow and mantle hydration on oceanic transform faults. *Earth and Planetary Science Letters*, *532*, 115988. doi: https://doi.org/10.1016/j.epsl.2019.115988

Ren, Y., Geersen, J., & Grevemeyer, I. (2022). Impact of spreading rate and age-offset on oceanic transform fault morphology. *Geophysical Research Letters*, *49*(2), e2021GL096170. doi: https://doi.org/10.1029/2021GL096170

Richards-Dinger, K. B., & Shearer, P. M. (2000). Earthquake locations in southern California obtained using source-specific station terms. *Journal of Geophysical Research: Solid Earth*, *105*(B5), 10939-10960. doi: https://doi.org/10.1029/2000JB900014

Roland, E., Behn, M. D., & Hirth, G. (2010). Thermal-mechanical behavior of oceanic transform faults: Implications for the spatial distribution of seismicity. *Geochemistry, Geophysics, Geosystems*, *11*(7). doi: https://doi.org/10.1029/2010GC003034

Roland, E., Lizarralde, D., McGuire, J. J., & Collins, J. A. (2012). Seismic velocity constraints on the material properties that control earthquake behavior at the Quebrada-Discovery-Gofar transform faults, East Pacific Rise. *Journal of Geophysical Research: Solid Earth*, *117*(B11). doi: https://doi.org/10.1029/2012JB009422

Ross, Z. E., & Cochran, E. S. (2021). Evidence for latent crustal fluid injection transients in Southern California from long-duration earthquake swarms. *Geophysical Research Letters*, *48*(12), e2021GL092465.

Ross, Z. E., Cochran, E. S., Trugman, D. T., & Smith, J. D. (2020). 3D fault architecture controls the dynamism of earthquake swarms. *Science*, *368*(6497), 1357–1361.

Ruppert, N., Barcheck, G., & Abers, G. (2021). *Aacse earthquake catalog: January-august, 2019.* Retrieved from `http://hdl.handle.net/11122/11967`

Saragiotis, C., Hadjileontiadis, L., & Panas, S. (2002). PAI-S/K: A robust automatic seismic P phase arrival identification scheme. *IEEE Transactions on Geoscience and Remote Sensing*, *40*(6), 1395-1404. doi: 10.1109/TGRS.2002.800438

Savage, J. C., & Prescott, W. H. (1978). Asthenosphere readjustment and the earthquake cycle. *Journal of Geophysical Research: Solid Earth*, *83*(B7), 3369-3376. doi: https://doi.org/10.1029/JB083iB07p03369

Scholz, C. H. (1998). Earthquakes and friction laws. *Nature*, *391*(6662), 37-42. Retrieved from `https://doi.org/10.1038/34097` doi: 10.1038/34097

Scholz, C. H., Tan, Y. J., & Albino, F. (2019). The mechanism of tidal triggering of earthquakes at mid-ocean ridges. *Nature communications*, *10*(1), 1–7.

Searle, R. C. (1986). GLORIA investigations of oceanic fracture zones: comparative study of the transform fault zone. *Journal of the Geological Society*, *143*(5), 743–756. doi: 10.1144/gsjgs.143.5.0743

Segall, P., & Lu, S. (2015). Injection-induced seismicity: Poroelastic and earthquake nucleation effects. *Journal of Geophysical Research: Solid Earth*, *120*(7), 5082-5103. doi: https://doi.org/10.1002/2015JB012060

Shelly, D. R. (2009). Possible deep fault slip preceding the 2004 Parkfield earthquake, inferred from detailed observations of tectonic tremor. *Geophysical Research Letters*, *36*(17). doi: https://doi.org/10.1029/2009GL039589

Shelly, D. R., Peng, Z., Hill, D. P., & Aiken, C. (2011). Triggered creep as a possible mechanism for delayed dynamic triggering of tremor and earthquakes. *Nature Geoscience*, *4*(6), 384–388.

Shi, P., Wei, M. M., & Pockalny, R. A. (2021). The ubiquitous creeping segments on oceanic transform faults. *Geology*. doi: 10.1130/G49562.1

Stein, R. S., Barka, A. A., & Dieterich, J. H. (1997, 03). Progressive failure on the North Anatolian fault since 1939 by earthquake stress triggering. *Geophysical Journal International*, *128*(3), 594-604. doi: 10.1111/j.1365-246X.1997.tb05321.x

Stroup, D. F., Bohnenstiehl, D. R., Tolstoy, M., Waldhauser, F., & Weekly, R. T. (2007). Pulse of the seafloor: Tidal triggering of microearthquakes at 9°50'n east pacific rise. *Geophysical Research Letters*, *34*(15). doi: https://doi.org/10.1029/2007GL030088

Stroup, D. F., Tolstoy, M., Crone, T. J., Malinverno, A., Bohnenstiehl, D. R., & Waldhauser, F. (2009). Systematic along-axis tidal triggering of microearthquakes observed at 9°50'N East Pacific Rise. *Geophysical Research Letters*, *36*(18). doi: https://doi.org/10.1029/2009GL039493

Sykes, L. R., & Ekström, G. (2012). Earthquakes along Eltanin transform system, SE Pacific Ocean: fault segments characterized by strong and poor seismic coupling and implications for long-term earthquake prediction. *Geophysical Journal International*, *188*(2), 421-434. doi: 10.1111/j.1365-246X.2011.05284.x

Tebbens, S. F., & Cande, S. C. (1997). Southeast pacific tectonic evolution from early oligocene to present. *Journal of Geophysical Research: Solid Earth*, *102*(B6), 12061-12084. doi: https://doi.org/10.1029/96JB02582

Trugman, D. T., & Shearer, P. M. (2017). GrowClust: A hierarchical clustering algorithm for relative earthquake relocation, with application to the Spanish Springs and Sheldon, Nevada, earthquake sequences. *Seismological Research Letters*, *88*(2A), 379-391.

Trugman, D. T., Shearer, P. M., Borsa, A. A., & Fialko, Y. (2016). A comparison of long-term changes in seismicity at The Geysers, Salton Sea, and Coso geothermal fields. *Journal of Geophysical Research: Solid Earth*, *121*(1), 225–247.

van der Elst, N. J., Savage, H. M., Keranen, K. M., & Abers, G. A. (2013). Enhanced remote earthquake triggering at fluid-injection sites in the midwestern united states. *Science*, *341*(6142), 164-167. doi: 10.1126/science.1238948

Vidale, J. E., Ellsworth, W. L., Cole, A., & Marone, C. (1994). Variations in rupture process with recurrence interval in a repeated small earthquake. *Nature*, *368*(6472), 624-626. doi: 10.1038/368624a0

Wang, J., Xu, C., Freymueller, J. T., Wen, Y., & Xiao, Z. (2021). AutoCoulomb: An automated configurable program to calculate Coulomb stress changes on receiver faults with any orientation and its application to the 2020 Mw7.8 Simeonof Island, Alaska, earthquake. *Seismological Research Letters*, *92*(4), 2591-2609. doi: 10.1785/0220200283

Wang, R., Schmandt, B., Zhang, M., Glasgow, M., Kiser, E., Rysanek, S., & Stairs, R. (2020). Injection-induced earthquakes on complex fault zones of the Raton basin illuminated by machine-learning phase picker and dense nodal array. *Geophysical Research Letters*, *47*(14), e2020GL088168. doi: https://doi.org/10.1029/2020GL088168

Wesnousky, S. G. (2008). Displacement and geometrical characteristics of earthquake surface ruptures: Issues and implications for seismic-hazard analysis and the process of earthquake rupture. *Bulletin of the Seismological Society of America*, *98*(4), 1609–1632.

Whitmarsh, R. B., & Calvert, A. J. (1986). Crustal structure of Atlantic fracture zones — I. The Charlie-Gibbs Fracture Zone. *Geophysical Journal International*, *85*(1), 107-138. doi: 10.1111/j.1365-246X.1986.tb05174.x

Wiemer, S., & Wyss, M. (2000). Minimum magnitude of completeness in earthquake catalogs: Examples from alaska, the western united states, and japan. *Bulletin of the Seismological Society of America*, *90*(4), 859–869.

Wirth, E. A., Sahakian, V. J., Wallace, L. M., & Melnick, D. (2022). The occurrence and hazards of great subduction zone earthquakes. *Nature Reviews Earth & Environment*, *3*(2), 125-140. doi: 10.1038/s43017-021-00245-w

Wolfson-Schwehr, M., & Boettcher, M. S. (2019). Global characteristics of oceanic transform fault structure and seismicity. In J. C. Duarte (Ed.), *Transform plate boundaries and fracture zones* (p. 21–59). Amsterdam: Elsevier.

Wolfson-Schwehr, M., Boettcher, M. S., McGuire, J. J., & Collins, J. A. (2014). The relationship between seismicity and fault structure on the Discovery transform fault, East Pacific Rise. *Geochemistry, Geophysics, Geosystems*, *15*(9), 3698-3712. doi: https://doi.org/10.1002/2014GC005445

Yu, Z., Singh, S. C., Gregory, E. P. M., Maia, M., Wang, Z., & Brunelli, D. (2021). Semibrittle seismic deformation in high-temperature mantle mylonite shear zone along the Romanche transform fault. *Science Advances*, *7*(15), eabf3388. doi: 10.1126/sciadv.abf3388

Zhang, M., Ellsworth, W. L., & Beroza, G. C. (2019). Rapid earthquake association and location. *Seismological Research Letters*, *90*(6), 2276-2284.

Supplementarry materials for "Seismicity, fault architecture, and slip mode of the westernmost Gofar transform fault"

Jianhua Gong[1] **& Wenyuan Fan**[1]

[1]Scripps Institution of Oceanography, UC San Diego, La Jolla, California 92093, USA

Content

- Text S1–2
- Table S1–3
- Figure S1–14

Corresponding author: Jianhua Gong, `j4gong@ucsd.edu`

Text S1. Waveform Amplitudes, Magnitudes, and Missing Events

Waveform Amplitudes: We first examine the horizontal over vertical (H/V) amplitude ratios of records from each earthquake to assure that the stations recorded the events properly before computing the local magnitudes. We apply the same windowing procedure to process the S waves as detailed in the main text. A horizontal amplitude (H) is measured as the maximum amplitude of the root sum square of the two horizontal components of the S-wave window for each earthquake, and a vertical amplitude (V) is measured as the maximum amplitude of the vertical component of the S-wave window for the same event. The H/V amplitude ratio results are shown in Fig. S12 for each station respectively. If a station functioned properly during the deployment period, its H/V amplitude ratio would remain near constant for all earthquakes. Stations G01, G11, and G15 did not record useful data and we do not analyze their waveforms. G10 has H/V of a few thousand indicating that its Z component did not work properly. For the remaining stations, we find that H/V ratios of stations G02, G07, G09 and G12 changed abruptly after the 2008 M6 mainshock, while the other stations had consistent H/V ratio during the deployment. The sudden changes in H/V ratio for G02, G07, and G12 are likely related to the M6 event. G09 is likely broken after 170 days as well. Therefore, amplitude measurements at G02, G07, G09 and G12 are not used in our magnitude calculation after Julian day 262, 262, 170, and 262 of 2008, respectively.

Estimating Local Magnitudes: The measured local magnitudes are unusually small (Fig. S3a). One possibility is that instrument gains may have not been well calibrated. Further, coefficients in Eq. 1 in the main text may not be suitable to characterize the geological structure at Gofar as they are empirically estimated for southern California. Therefore, we compare our measurements with 115 moment magnitudes from Moyer et al. (2018) that are derived using a spectra method. We estimate a static shift term $\hat{s}$ that minimizes the ℓ_2 misfit between the two sets of magnitude estimates:

$$\hat{s} = \arg\min_s \sum_i (\mathrm{M_W}(i) - \mathrm{M_L}(i) + s)^2$$

The best estimate is $\hat{s} = -0.65$ (Fig. S3b). Therefore, we shift the local magnitudes by 0.65. Some events in our automated catalog have large amplitudes but less than 5 S arrival picks. For these cases, we use predicted S arrival times instead and compute local magnitudes for these events using the same criteria as in the main text. This yields 299 more local magnitude estimates. Our catalog has a magnitude completeness of 0.6 and a b-value of 0.75 (Fig. S3c).

Identifying Missing Events: Visual inspection of daily waveforms suggests that there are missing events in our automated catalog that generated large amplitudes. To identify these missing events, we systematically scan continuous vertical component waveforms to search for large amplitude signals. We first define an amplitude threshold and examine all signals that exceed the threshold. The amplitude threshold, A_t, is obtained from the automated catalog:

$$A_t = \arg 10 \times \min_i(\max_j(A_{ij}))$$

where A_{ij} is the maximum vertical S wave amplitude of the ith event on station j in a time window 1 s before and 5 s after the S arrival. The S-waveforms are bandpass filtered between 4 and 12 Hz to measure A_{ij}. The above equation leads to a threshold of 74,866 in unit count, which is $\sim 1.2 \times 10^{-4}$ m/s for the instruments. We mute the waveforms of earthquakes in the automated catalog (30 s zero-value window from the origin times) and search the rest continuous waveforms to identify possible missing events. Once a signal is detected on a certain station, we window 12 s before and 18 s after the detected signal for all stations and save the records as from a potential earthquake. The procedure leads to 1,390 potential events. We then visually inspect these potential earthquakes and remove false detections. We manually pick P and S wave arrival times of the true detections, grid search their locations, and determine their local magnitudes using the procedure described in the main text. In total, we successful identify and locate 397 more events and compute local magnitudes for 231 events. The depth distribution of these events are shown in Fig. S9.

Text S2. GrowClust Input Parameters and Earthquake Clustering

Several parameters in the GrowClust input files can influence the earthquake relocation results and clustering, including

- `rmin`: the minimum permissible cross-correlation coefficient for differential times used in computing the event-pair similarity coefficients.
- `min_fraction`: the minimum permissible fraction of connected event pairs between two clusters to merge the clusters. Connected event pairs have similarity coefficients greater than `rmin`.
- `rmsmax`: the maximum permissible root-mean-square (rms) differential time residual to merge two clusters.
- `rmedmax`: the maximum permissible median differential time residual to merge two clusters.
- `max_horz/vert_shift`: the maximum permissible horizontal or vertical centroid shift to merge two clusters.

We test seven sets of input parameters to examine the effects of the parameters on the relocation results. The parameter values of the tests are shown in Table. S3. The cluster size (earthquake number) of the top 50 clusters for each test are shown in Fig. S13. The location and clustering results are shown in Fig. S4, S5, and S6. We set a minimum cluster size of 100 to evaluate the tests. Overall, `rmin` and `min_fraction` have strong impacts on the number of clusters and the total number of selected events. Parameters `rmsmax`, `rmedmax`, and `max_horz/vert_shift` influence details of the relocation results, such as the separation between shallow and deep events. We find that cluster 0 is present for all the tests and the events are likely near EPR, although earthquake locations of the cluster is not well constrained, limited by the current network configuration.

In general, we find the relocation results are stable except for extreme parameter values. Test 1 has the lowest `min_fraction` (0.001) leading to a total of 9 clusters (Fig. S4a and b), including 99% of the total seismicity (Table. S3). As GrowClust keeps the centroid location of each cluster invariant during the relocation procedure, this set of parameters would cause gap artifacts between earthquake strands (e.g., Cluster 8 for this test).

Test 2 has a `min_fraction` of 0.01, leading to 37 clusters, and each cluster has fewer events comparing to the ones of Test 1 (Table. S3). This set of parameters are better than those of Test 1 because off-fault seismicity are not merged with on-fault seismicity and artifacts are eliminated. Test 3 has a `max_vert_shift` of 1 (Table. S3), which would prevent GrowClust from merging two clusters with large vertical offset, and this set of parameters can effectively separate deep seismicity from shallow seismicity.

Test 4 constrains the `rmsmax` and `rmedmax` values (Table. S3), resulting in a decrease in the total selected events. Additionally, artifacts are present in the eastern part of the fault, which are likely caused by the large `max_vert_shift` value (Fig. S5a and b). Test 5 constrains `max_vert_shift`, `rmsmax`, and `rmedmax` (Table. S3). Similarly, there is a decrease in the total selected events (89%). However, artifacts in the eastern part of the fault are eliminated, showing effects of `max_vert_shift` (black circle in Fig. S5c). Test 6 shares a similar set of parameters as of Test 5 except that `rmin` is 0.8, which results in a increase in the cluster number (Table. S3). The strict set of parameters is effective in removing off-fault clusters or artifacts of seismicity strands albeit at a cost of including fewer events (Fig. S5e and f).

Test 7 has a `rmin` value of 0.6 and `max_horz/vert_shift` of 1 km, respectively (Table. S3), resulting in two off-fault clusters and no apparent artifacts between seismicity strands (Fig. S6). We prefer parameters of Test 7 because there are few off-fault clusters, no unrealistic fault step-overs, and the final relocation catalog includes 84% of the total seismicity. The set of parameters are used for our analysis in the main text. For Test 7, 34 clusters have more than 100 events, respectively. They are indexed as 0 to 33 sorted by the centroid longitude of the events in each cluster, detailed in Table S2, Fig. S14, and Fig. S6. The daily seismicity rates of each cluster are shown in Fig. S7.

References

Moyer, P. A., Boettcher, M. S., McGuire, J. J., & Collins, J. A. (2018). Spatial and Temporal Variations in Earthquake Stress Drop on Gofar Transform Fault, East Pacific Rise: Implications for Fault Strength. *Journal of Geophysical Research: Solid Earth*, *123*(9), 7722-7740. doi: https://doi.org/10.1029/2018JB015942

Table S1. Information of Gofar OBS stations. SG: collocated strong motion sensors

Name	lat/lon/dep (m)	SG	Sample Rate	Function	Upsampling Factor
G01	-4.4516/-106.260498/-3209.0		100		
G02	-4.5465/-106.199203/-3050.0		100	Y	4
G03	-4.6161/-106.149803/-3187.0		100	Y	4
G04	-4.5553/-106.126602/-3170.0	Y	50	Y	4
G05	-4.4907/-106.080101/-3558.0	Y	50	Y	2
G06	-4.5694/-106.035896/-3601.0	Y	50	Y	2
G07	-4.6591/-105.968498/-3195.0	Y	50	Y	1
G08	-4.5962/-105.948097/-3358.0	Y	50	Y	4
G09	-4.5022/-105.909698/-3258.0	Y	50	Y	1
G10	-4.5932/-105.866898/-3395.0	Y	50	Y	1
G11	-4.6205/-105.791702/-3238.0		100		
G12	-4.6778/-105.800003/-3192.0		100	Y	4
G13	-4.5400/-105.706497/-3402.0		100	Y	4
G14	-4.6051/-105.70240 /-3926.0		100	Y	4
G15	-4.6566/-105.600899/-3313.0		100		
G16	-4.7169/-105.584198/-2961.0		100	Y	2

Table S2. Seismicity clusters.

Cluster ID	Event Number	Centroid lat/lon/dep (km)	Zone/Group ID	Notes
0	146	-4.5778/-106.3001/-5.72		Not well located
1	145	-4.5259/-106.2468/-3.95	Zone 5 Group 1	
2	633	-4.5137/-106.2339/-5.51	Zone 5 Group 1	
3	1134	-4.5147/-106.2328/-3.95	Zone 5 Group 1	
4	111	-4.5157/-106.2289/-2.57	Zone 5 Group 1	
5	1045	-4.5152/-106.2195/-3.41	Zone 5 Group 1	
6	1324	-4.5170/-106.2175/-5.60	Zone 5 Group 1	
7	1366	-4.5244/-106.2058/-4.31	Zone 5 Group 2	
8	823	-4.5240/-106.1912/-6.02	Zone 5 Group 1	
9	178	-4.5559/-106.1907/-5.36		Not well located
10	895	-4.5252/-106.1741/-5.20	Zone 4 Group 3	
11	636	-4.5368/-106.1512/-6.73	Zone 4 Group 2	
12	539	-4.5385/-106.1416/-4.69	Zone 4 Group 2	
13	499	-4.5434/-106.1226/-6.34	Zone 4 Group 2	
14	1070	-4.5379/-106.1070/-4.76	Zone 4 Group 1	
15	807	-4.5512/-106.0609/-5.07	Zone 3 Group 1	
16	101	-4.5550/-106.0557/-8.64	Zone 3 Group 3	
17	1173	-4.5570/-106.0377/-4.88	Zone 3 Group 1	
18	2120	-4.5622/-105.9962/-5.46	Zone 3 Group 1	
19	714	-4.5715/-105.9703/-7.52	Zone 3 Group 2	
20	992	-4.5692/-105.9634/-5.29	Zone 2 Group 1	
21	1358	-4.5785/-105.9572/-7.30	Zone 2 Group 2	
22	1191	-4.5766/-105.9374/-3.94	Zone 2 Group 1	
23	110	-4.5716/-105.9373/-6.75	Zone 2 Group 2	
24	1116	-4.5828/-105.9325/-7.14	Zone 2 Group 3	
25	1349	-4.5812/-105.9205/-4.36	Zone 2 Group 1	
26	801	-4.5864/-105.9103/-7.22	Zone 2 Group 3	
27	913	-4.5812/-105.9100/-3.12	Zone 2 Group 1	
28	538	-4.5927/-105.8639/-4.91	Zone 1 Group 1	
29	484	-4.6053/-105.8186/-6.60	Zone 1 Group 1	
30	106	-4.6090/-105.7779/-6.40	Zone 1 Group 1	
31	631	-4.6176/-105.7672/-8.96	Zone 1 Group 2	
32	113	-4.6352/-105.7008/-9.18	Zone 1 Group 2	
33	809	-4.6326/-105.6779/-7.43	Zone 1 Group 1	

Table S3. Input parameters for GrowClust.

Test	rmin	min fraction	rmsmax rmedmax	max H/V shifts	cluster num	eq percent
1	0.6	0.001	99,99	99, 5	9	99%
2	0.6	0.01	99,99	99, 5	37	97%
3	0.6	0.01	99,99	99, 1	38	97%
4	0.6	0.01	0.4,0.05	99, 5	43	94%
5	0.6	0.01	0.4,0.05	99, 1	40	89%
6	0.8	0.01	0.4,0.05	99, 1	56	68%
7	0.6	0.01	0.4,0.05	1, 1	34	84%

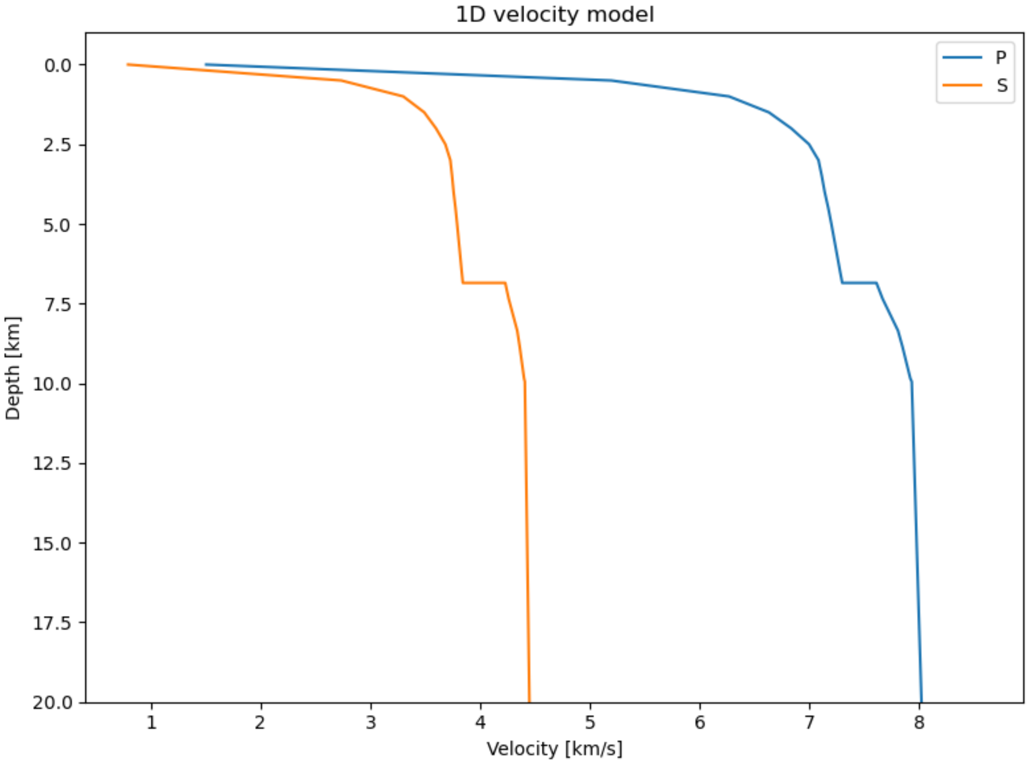

Figure S1. One dimensional P and S velocity model that are used for earthquake locations.

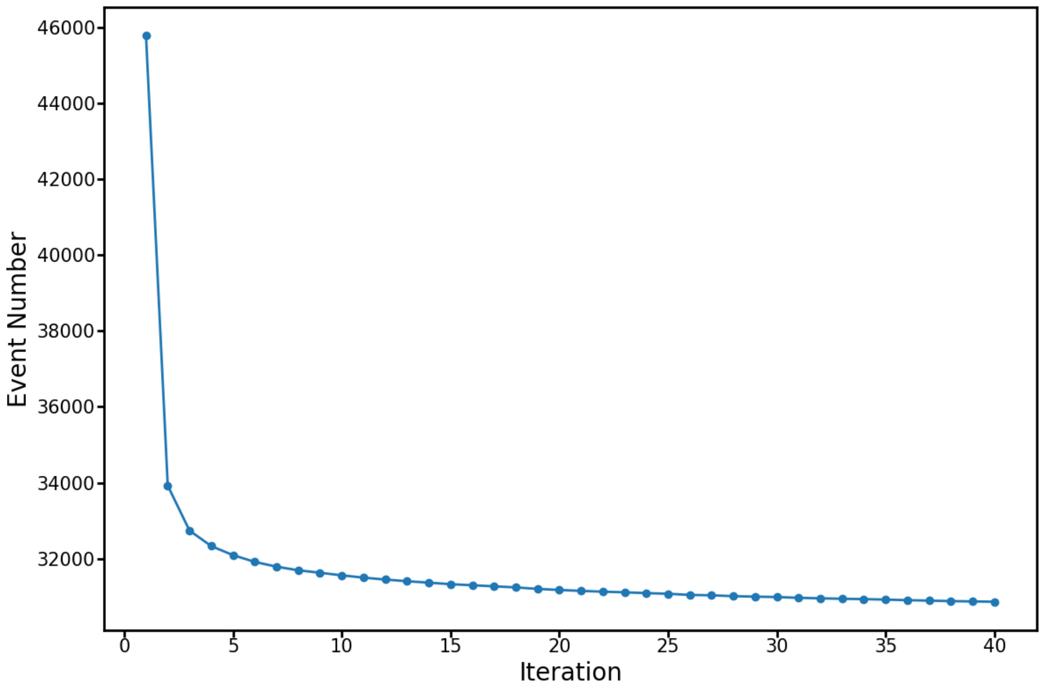

Figure S2. L-curve of earthquake numbers after each COMPLOC iteration.

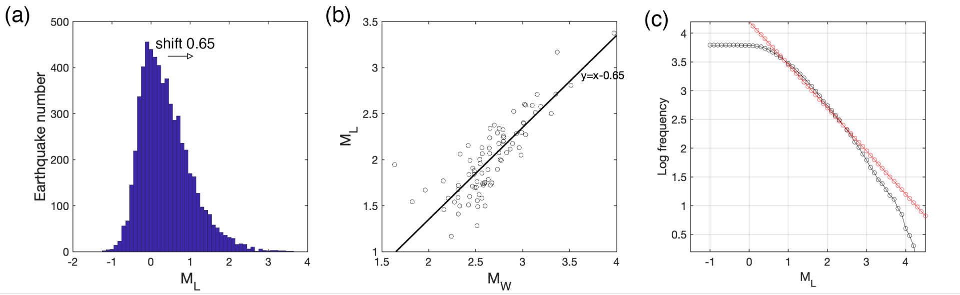

Figure S3. Gofar seismicity statistics. (a) Histogram of the local magnitudes. (b) Comparison between the local magnitude estimates and moment magnitude estimates from Moyer et al. (2018) for 115 common events. Black solid line denotes $y = x - 0.65$. (c) Magnitude-frequency distribution of the Gofar earthquakes. The horizontal axis is the corrected local magnitude and the vertical axis is the cumulative earthquake number in $\log_{10}$ scale. Straight line denotes a b-value of 0.75.

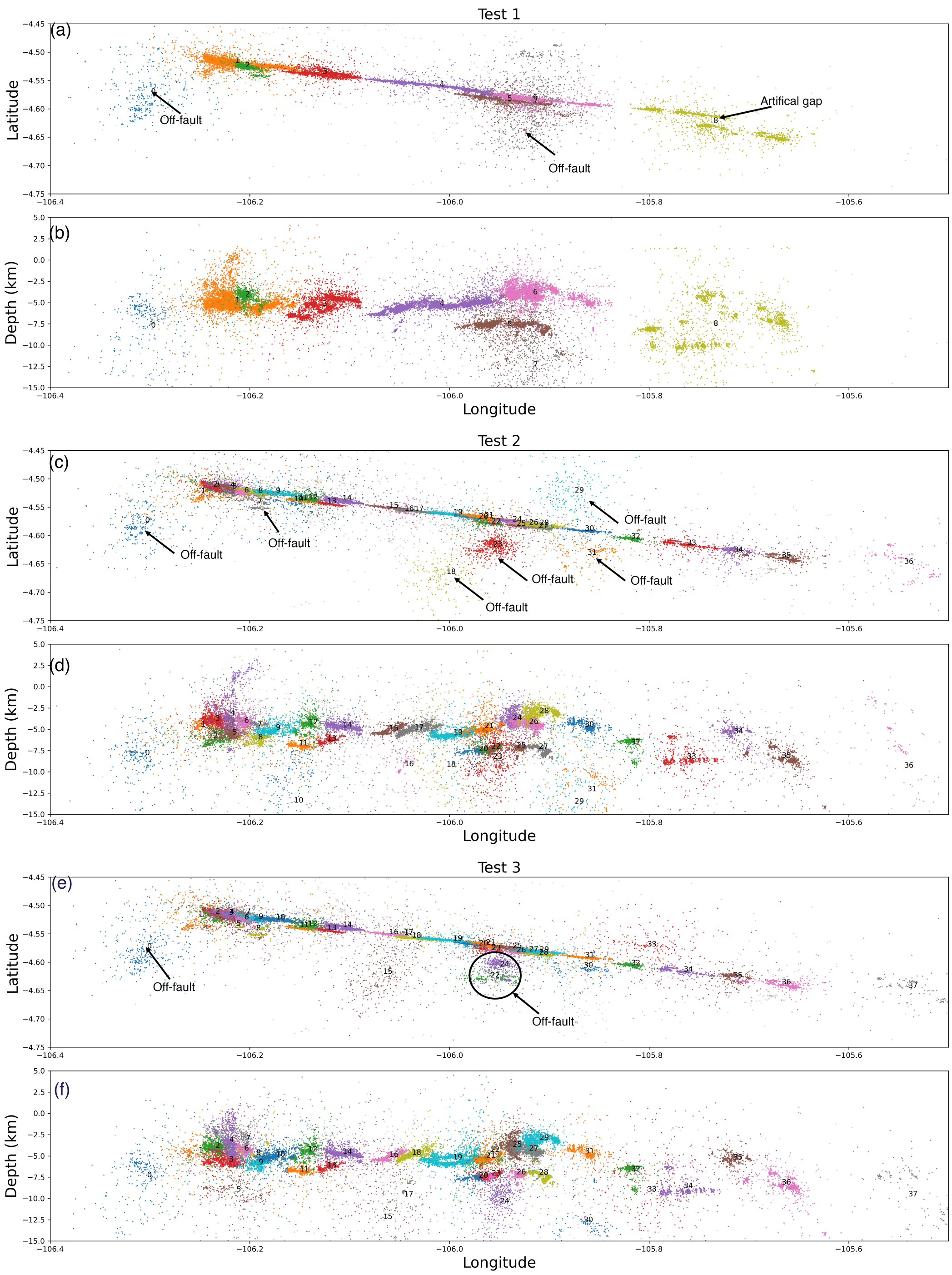

Figure S4. Comparison of relocation results for Test 1 to 3.

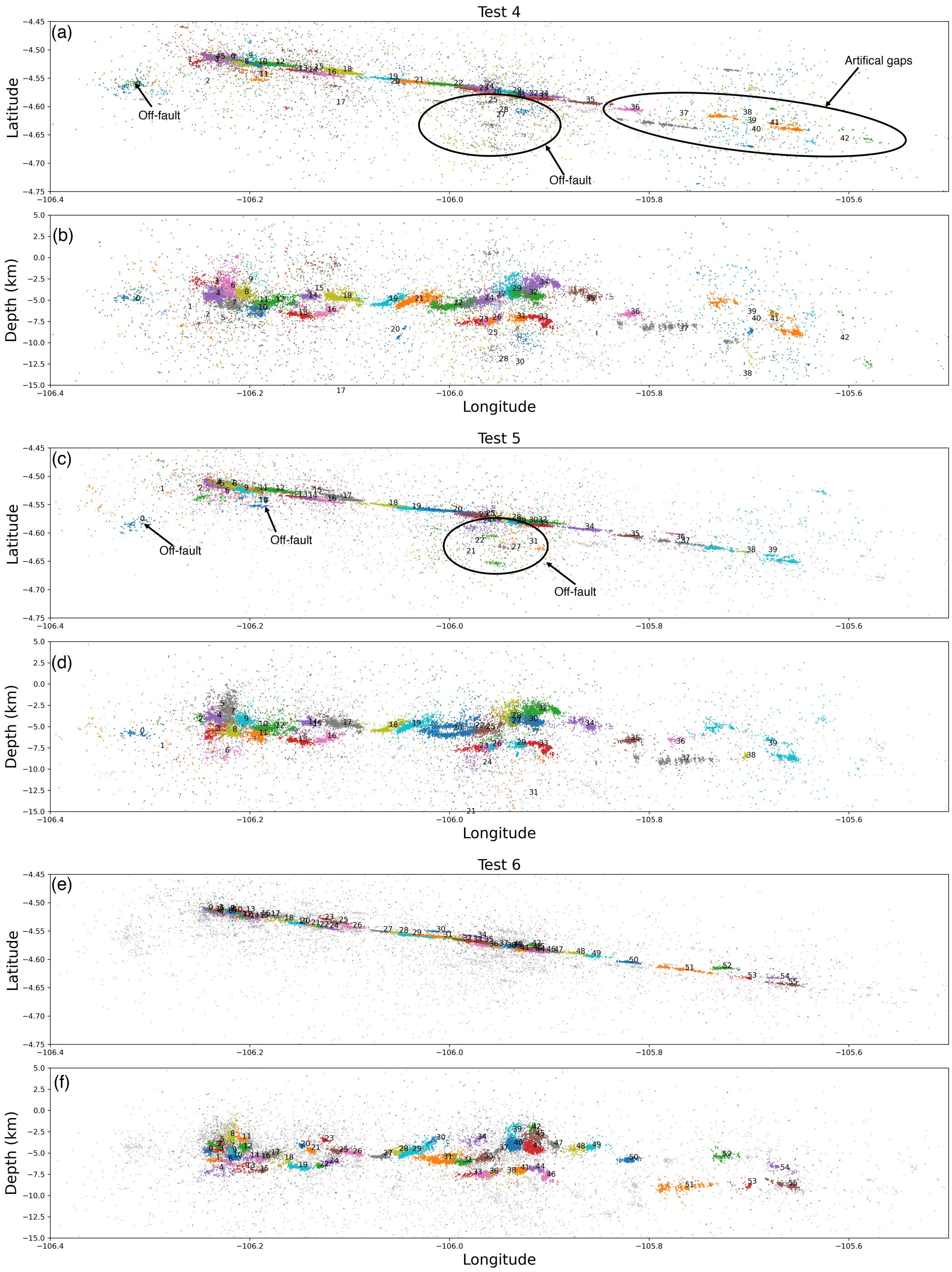

Figure S5. Comparison of relocation results for Test 4 to 6.

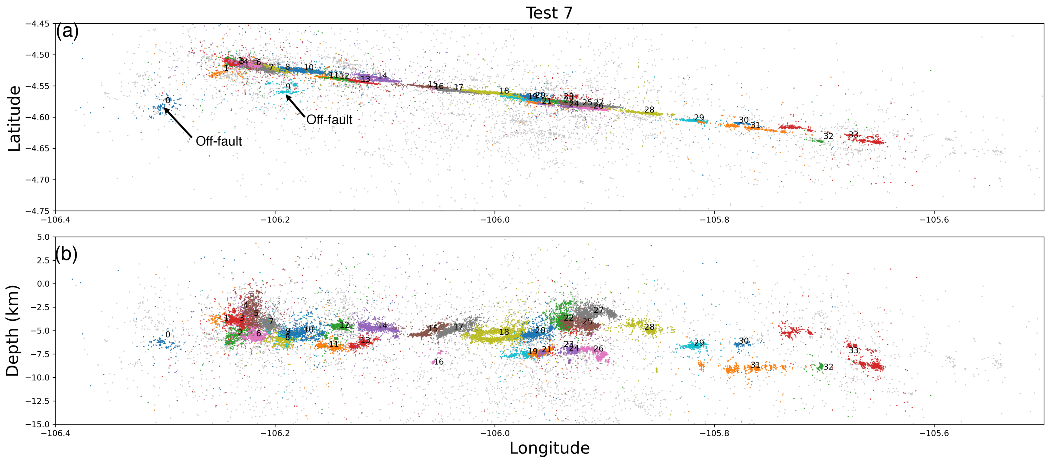

Figure S6. Relocated earthquakes of each cluster in map (a) and depth (b) views. The results are from using parameters of Test 7 (Table. S3).

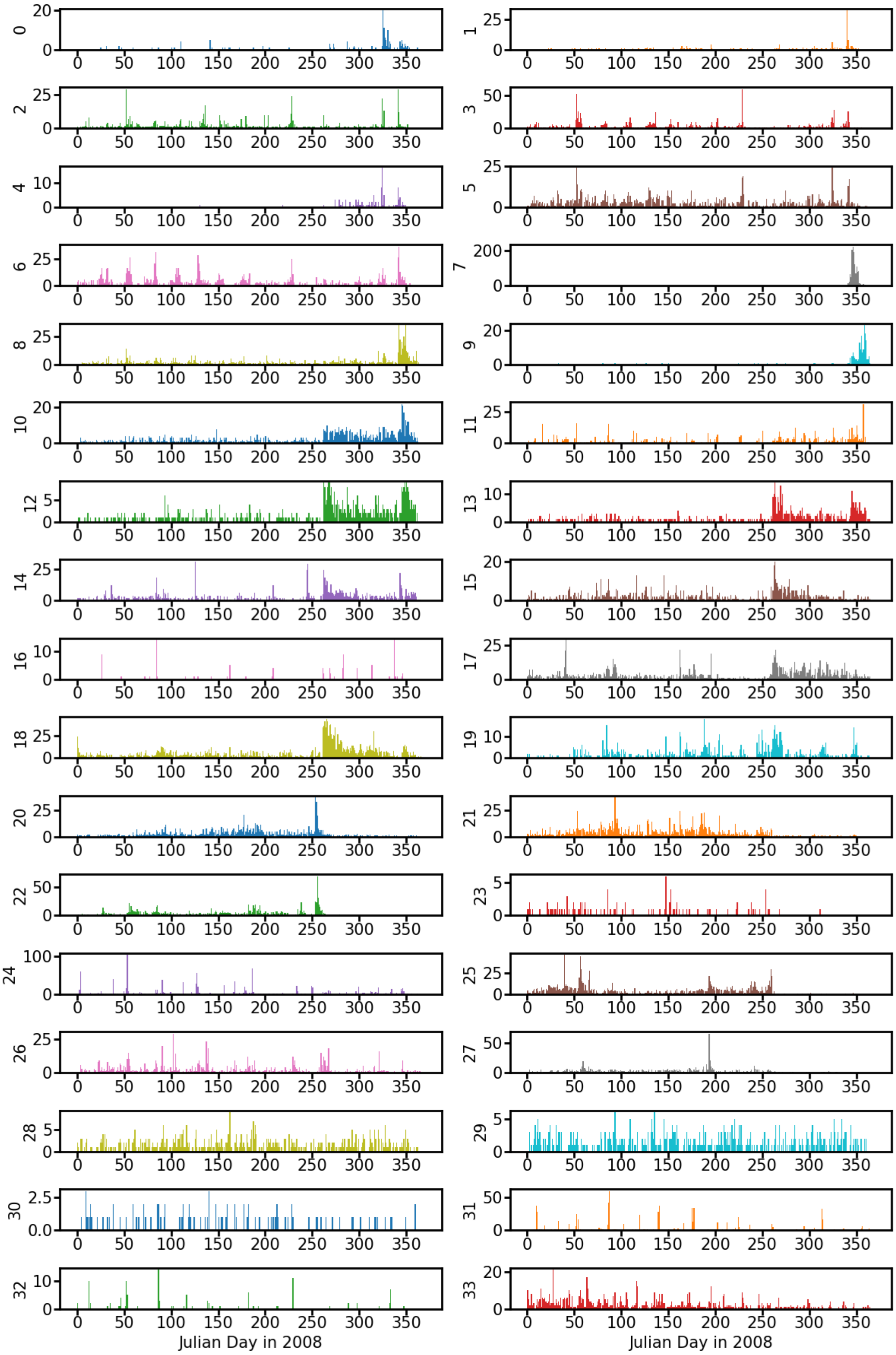

Figure S7. Daily seismicity rate of each cluster. The results are from using parameters of Test 7 (Table. S3).

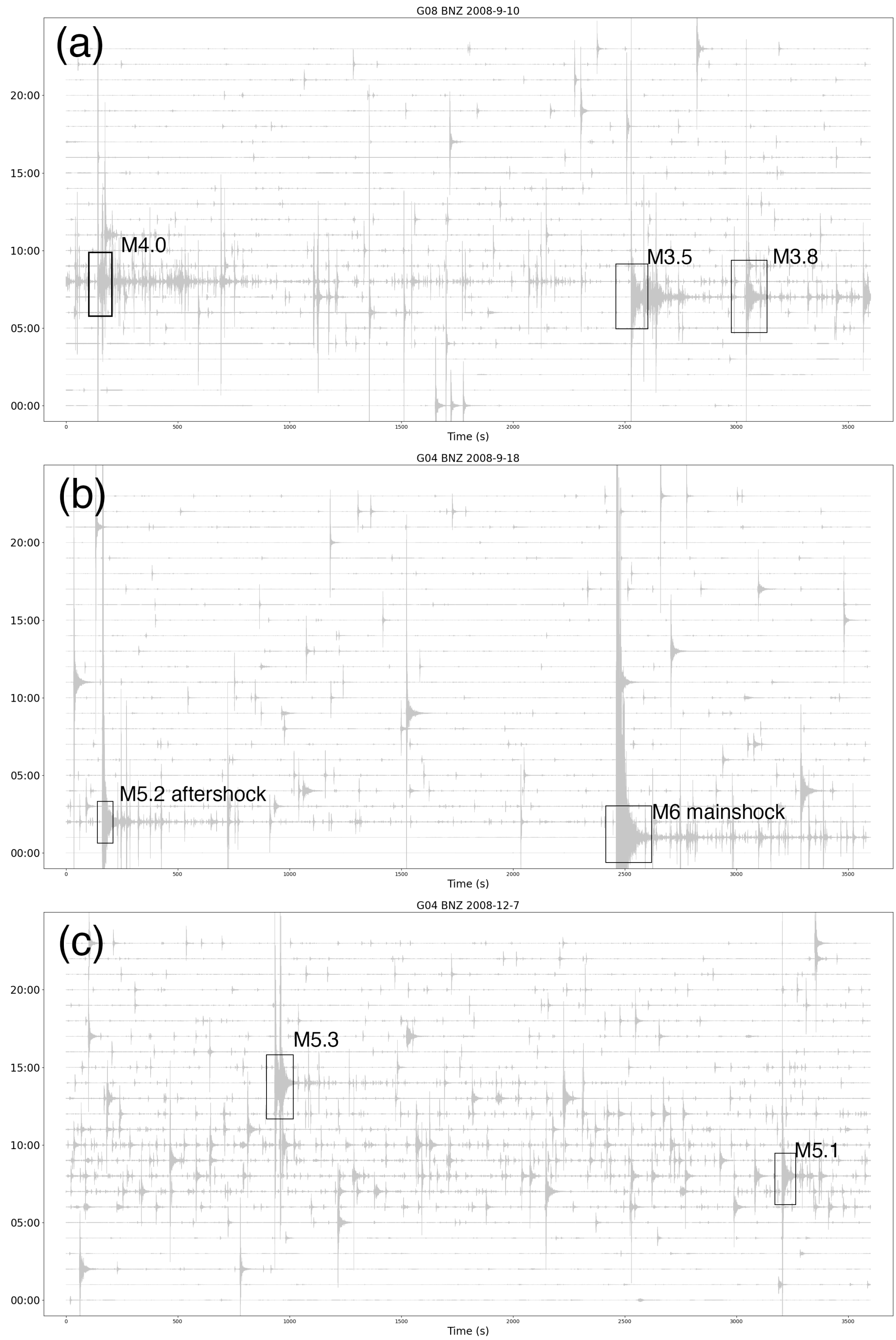

Figure S8. Example daily vertical waveforms for missing larger magnitude events at station G08 (2008-09-10, a) and G04 (2008-09-18, b; 2008-12-07, c). The missing events are highlighted by black rectangular boxes.

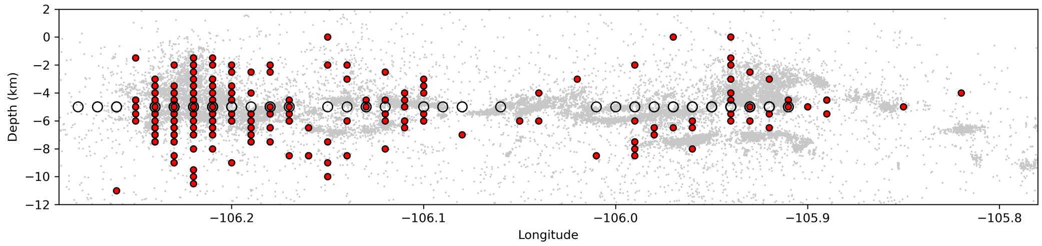

Figure S9. Manually located earthquakes (red solid circles and black open circles) in depth view. Black open circles denote 117 earthquakes whose depths assigned at 5 km.

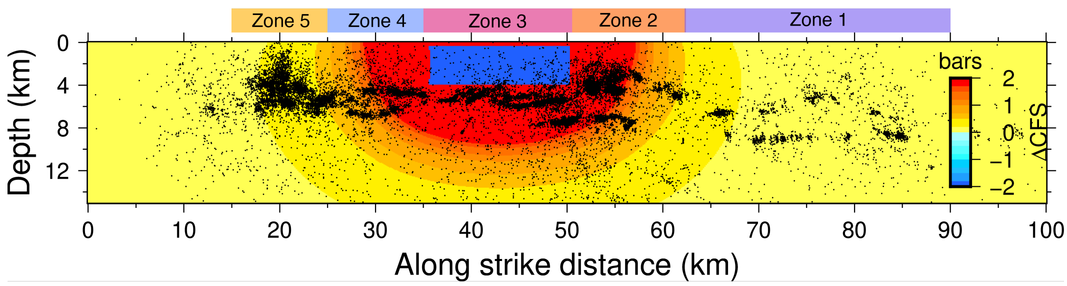

Figure S10. Coulomb stress changes due to the M6 mainshock on the assumed fault plane. Black dots are earthquakes from the GrowClust catalog.

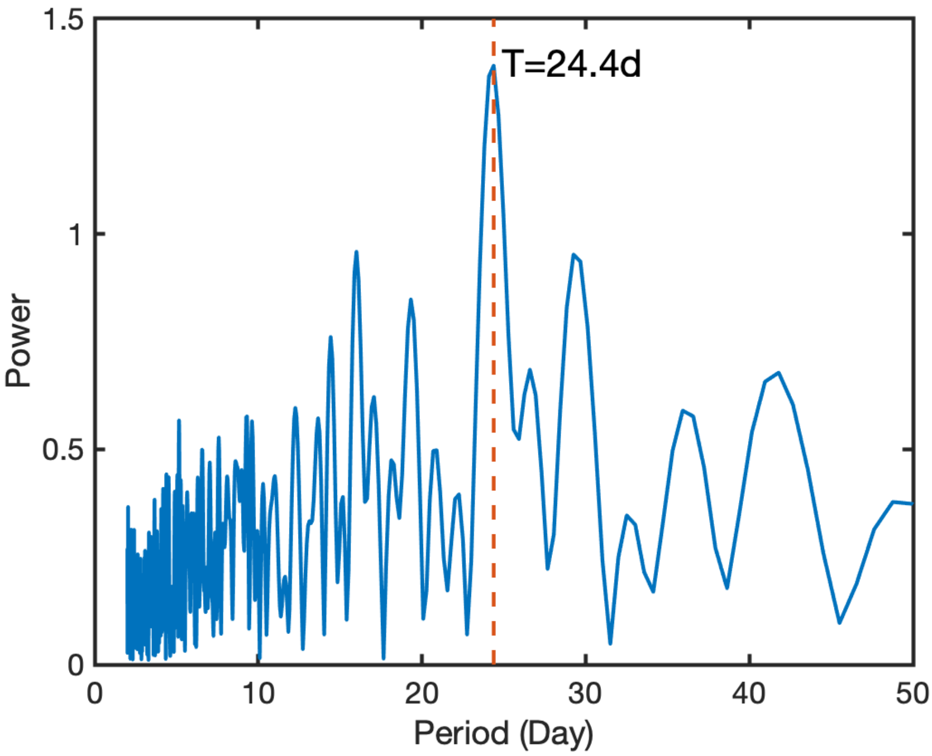

Figure S11. Spectrum of daily seismicity rate of Zone 5. The dash line indicates the peak period.

.

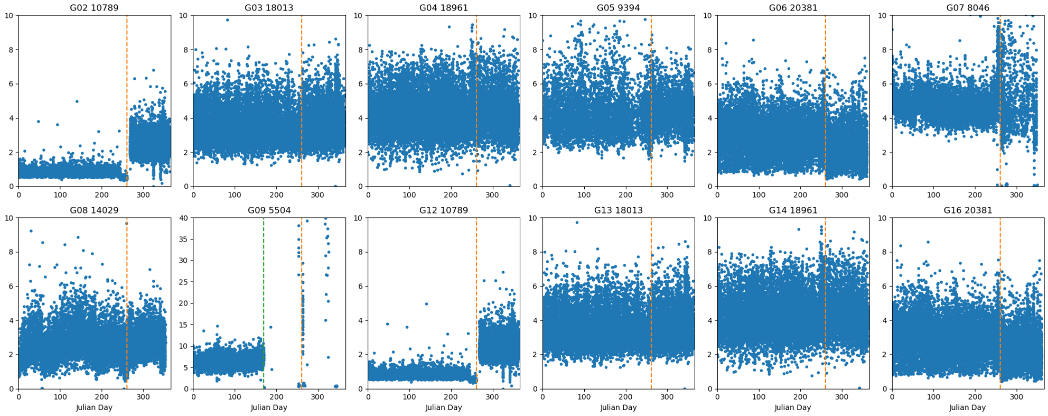

Figure S12. Amplitude ratio of horizontal/vertical (H/V) components. Orange dash lines indicate the occurrence time of the M6 mainshock. Green dashed line in the G09 panel indicates day 170. Panel titles show the station name and number of H/V measurements at that station.

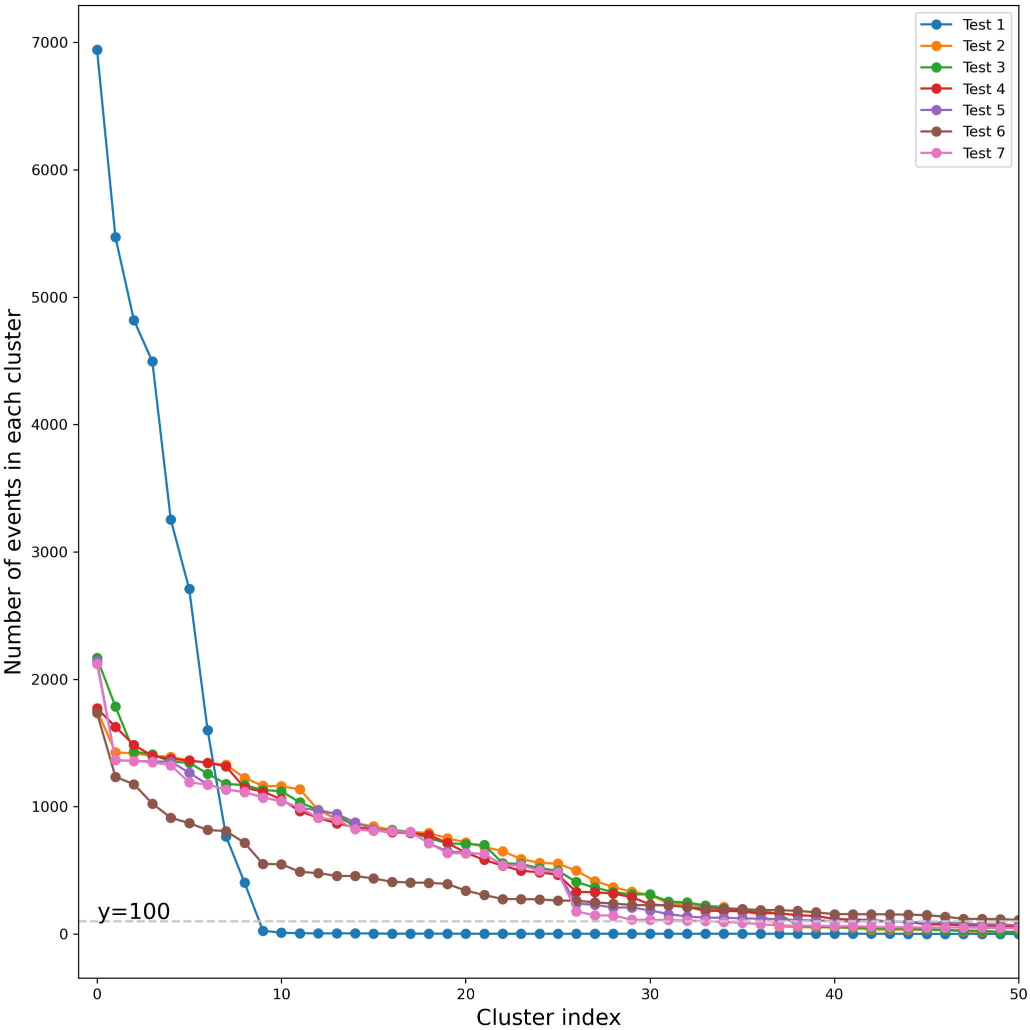

Figure S13. Earthquake numbers of the top 50 clusters of the seven tests.

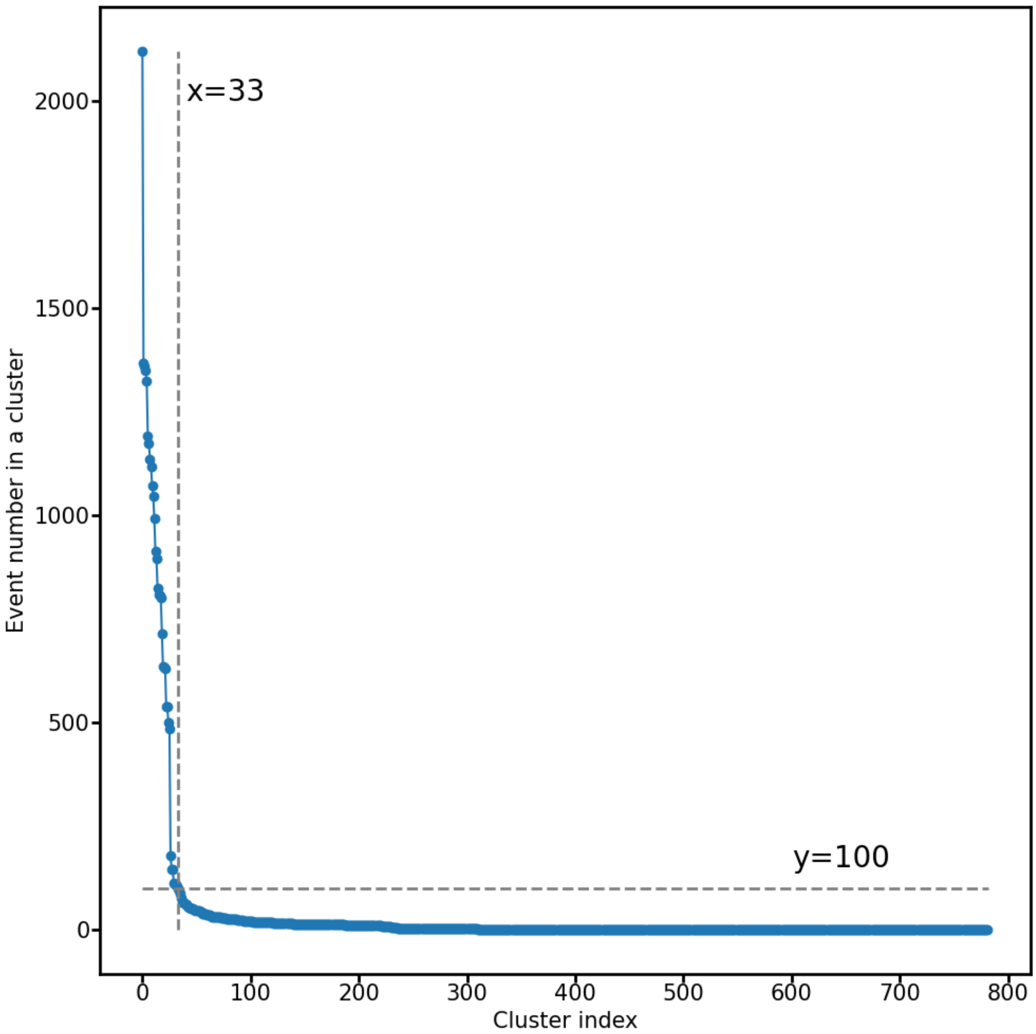

Figure S14. Earthquake numbers of clusters of Test 7.